

NUCLEAR MAGNETISM AND NEGATIVE
TEMPERATURES IN SILVER

By

PAUL LEE MOYLAND

A DISSERTATION PRESENTED TO THE GRADUATE SCHOOL
OF THE UNIVERSITY OF FLORIDA IN PARTIAL FULFILLMENT
OF THE REQUIREMENTS FOR THE DEGREE OF
DOCTOR OF PHILOSOPHY

UNIVERSITY OF FLORIDA

1997

© Copyright 1997

by

Paul Lee Moyland

To my friends and enemies.

ACKNOWLEDGEMENTS

I would like to thank Yasu Takano for putting up with me these past years. His patience and understanding have contributed greatly to this work.

I would like to thank the members of my supervisory committee for reviewing this work, and in particular, Pradeep Kumar for many useful discussions on magnetism and life in general.

The post-docs I have worked with have been many, and I owe them all a great debt. Dr. Jingwei Xu contributed to the design of the cryostat, and this experiment. Without his expertise, none of this would have worked.

Dr. Tien Lang has helped in most phases of this work. I thank him for graduating so that I could get my experiment done. Special thanks are due Greg Labbe and Brian Lothrop, who provided liquid helium even when I didn't want any. I thank the machine shop crew for their skill in deciphering my mechanical drawings. I thank Big Larry and Skinny Larry for their help on all things electronic (and a few things that were not...), along with Paul Stryder, Dennis Dent, and Jeff Legg. To John Mocko, special thanks for providing computer support so that I could write this up.

I thank Professors Mark Meisel, E. Dwight Adams, Gary Ihas, and Neil Sullivan for their assistance through the years. They have provided a good deal of aid and equipment (sometimes unknowingly) during my stay.

Many thanks to Dr. Richard P. Haley for proofreading my thesis. Any typos should be brought to his attention. Of course, final thanks has to be given to Kathleen Ellis, without whom the whole place would collapse.

This work was supported in part by the National Science Foundation, Grant No. DMR-8902538, and by an award from Research Corporation.

TABLE OF CONTENTS

ACKNOWLEDGEMENTS	iv
LIST OF TABLES	viii
LIST OF FIGURES	ix
ABSTRACT	xi
CHAPTERS	
1 INTRODUCTION	1
1.1 Nuclear Magnetism in the Noble Metals	2
1.2 Nuclear Magnetic Ordering in Metals	3
1.3 Negative Spin Temperatures	9
2 EXPERIMENTAL DESIGN AND TECHNIQUES	13
2.1 Cryostat	13
2.2 Silver Stage	16
2.3 NMR Coils and Electronics	19
2.4 Thermometry	23
2.5 Experimental Procedures	27
3 THEORETICAL CONSIDERATIONS AND EXPERIMENTAL RE- SULTS	32
3.1 Modified Bloch Equation	32
3.2 Spin-flip Equations of Motion	39
3.3 Data Reduction	44
3.4 Spin-flip Results	49
4 FUTURE WORK AND CONCLUSIONS	52
4.1 Higher Initial Polarization	52
4.2 Conclusions	53

APPENDICES

A	SUSCEPTIBILITY MEASUREMENT OF PRBE_{13}	54
A.1	Introduction	54
A.2	Mean Field Calculation for T_N	58
B	CW NMR MEASUREMENTS ON GOLD	64
B.1	Gold Fan Stage	64
B.2	NIST gold sample	66
B.3	Experimental Search	66
	REFERENCES	68
	BIOGRAPHICAL SKETCH	71

LIST OF TABLES

<u>Table</u>	<u>Page</u>
1.1 Nuclear magnetic properties of the noble metals.	3
2.1 Annealing results for silver foils.	18
2.2 Coil parameters	21
B.1 Annealing results for gold foils.	65

LIST OF FIGURES

<u>Figure</u>	<u>Page</u>
1.1 The composite system which is described in the text.	4
1.2 Phase diagram from reference [14], as described in the text.	7
1.3 Static magnetic susceptibility in zero field and 5 μ T as a function of spin polarization, from reference [14].	7
1.4 Schematic representation of the field inversion technique. Note that the gyromagnetic ratio in silver is negative. Therefore, the spin is anti-parallel to the magnetic moments, which are depicted with arrows.	11
2.1 Cooling power of the dilution refrigerator.	15
2.2 Silver cross and sample geometry.	17
2.3 The relative orientation of the pick-up and excitation coils.	20
2.4 Electronic circuit for the silver experiment.	22
2.5 Electronic circuit for the melting curve thermometer.	24
2.6 Schematic diagram of the Pt NMR circuit.	26
2.7 Temperature of the bundle during the precool.	27
2.8 Predicted pre-cooling curve for the silver nuclei at 100 μ K in 6.7 T. . .	30
3.1 A frequency sweep at $B = 825.4 \mu$ T showing the downshift and sup- pression/enhancement of the silver signal as described in the text. The solid lines mark the unshifted resonance frequencies.	35
3.2 Relative signs of the ^{107}Ag and ^{109}Ag nuclear spins at the resonance frequencies.	37

3.3	Relation between the effective and static field. The Y and Y' -axes are the same, and point into the page.	42
3.4	The lock-in output before data reduction. The cosine and sine channels of the lock-in are denoted by $+$ and \bigcirc , respectively.	45
3.5	Processed data, as described in the text.	46
3.6	Data used to determine the horizontal static field calibration. Solid lines are the result of the fit described in the text.	47
3.7	Spectrum used to set the polarization calibration. The solid line is the fit described in the text.	48
3.8	Initial magnetizations at positive temperature for the tipping sequence. Solid line is a Lorentzian fit to the data, which gives $p = 0.27$	49
3.9	Spectrum after the tipping pulse described in the text. Solid line is a Lorentzian fit to the data, which gives $p = -0.22$	50
3.10	Final magnetizations at positive temperature for the tipping sequence. Solid line is a Lorentzian fit to the data, which gives $p = 0.16$	50
A.1	Silver platform and coils for the PrBe_{13} experiment.	55
A.2	Schematic of the electronics for the PrBe_{13} experiment.	57
A.3	Nuclear susceptibility of PrBe_{13} . Solid line is the non-linear least squares fit to the high temperature data from 5 to 20 mK. The ordering transition is shown in the inset.	59
A.4	Division of the cubic lattice into eight sub-lattices, as described in the text.	60
A.5	The ratio of the Weiss and Neel temperatures as a function of the mean field coefficients and the spin configurations for.	62

Abstract of Dissertation Presented to the Graduate School
of the University of Florida in Partial Fulfillment
of the Requirements for the Degree of
Doctor of Philosophy

NUCLEAR MAGNETISM AND NEGATIVE
TEMPERATURES IN SILVER

By

Paul Lee Moyland

May 1997

Chairman: Yasumasa Takano
Major Department: Physics

A high-purity silver sample was used as the second stage of a nuclear demagnetization cryostat. Continuous Wave Nuclear Magnetic Resonance (CW NMR) was used to study the spin dynamics of ^{107}Ag and ^{109}Ag nuclear moments in magnetic fields of typically $850\text{ }\mu\text{T}$ and nuclear spin temperatures of 100 nK . The frequency response of the magnetization showed an enhanced signal intensity at the ^{109}Ag mode, due to the antiferromagnetic coupling between the two isotopes, while the ^{107}Ag mode signal intensity was suppressed. A new technique for generating negative spin-temperatures was developed, using digitized pulses one to two periods in duration. The efficiency of this new procedure is significantly higher than that of previous methods used in similiar systems.

CHAPTER 1 INTRODUCTION

Nuclear magnetism in metals has been a very rich field of study for experimental and theoretical physics. These systems, however, cannot be studied using standard laboratory apparatus. The small size of the magnetic moments, and their weak interactions, call for experiments at ultra-low temperatures with extremely sensitive probes.

The characteristics of the noble metals (Cu, Ag, Au) makes them ideal candidates for studying nuclear magnetism in metals. The interactions of the nuclear moments in these systems are well characterized, and experiments [1, 2, 3] on these systems provide a clean test of many interesting magnetic phenomena.

As compared to electronic moment materials, the interactions in these systems are very small. By scaling the nuclear magneton to the Bohr magneton (which characterizes electronic magnetism), one finds

$$\frac{\mu_n}{\mu_B} = \frac{m_e}{m_n} \sim 10^{-3}, \quad (1.1)$$

so that the interactions between magnetic moments (which vary as μ^2) are about six orders of magnitude smaller than for electronic moments. While the temperature range of interest for electronic magnets is typically on the order of several Kelvins and higher, for nuclear magnets one has to work at μK or lower temperatures. This leads to the possibility of studying the nuclear spins not only in their ordered state [2], but also at negative spin temperatures [3], due to their long spin-lattice relaxation times.

1.1 Nuclear Magnetism in the Noble Metals

The Hamiltonian H for the nuclear spins in the noble metals is particularly simple, and enables comparison between theory and experiments. In finite magnetic field B_0 , it consists of the dipolar, indirect exchange (RK) [5], and Zeeman interactions between the nuclear moments. The three terms are of the form

$$H_{\text{dipolar}} = \frac{\mu_0 \hbar^2}{4\pi} \sum_{i < j} \left(\frac{\gamma_i \gamma_j}{r_{ij}^3} [\vec{I}_i \cdot \vec{I}_j - 3(\vec{I}_i \cdot \hat{r}_{ij})(\vec{I}_j \cdot \hat{r}_{ij})] \right), \quad (1.2)$$

$$H_{\text{RK}} = \eta \frac{\mu_0 \hbar^2}{4\pi} \sum_{i < j} \left[\frac{\gamma_i \gamma_j}{r_{ij}^3} f(2k_F r_{ij}) \vec{I}_i \cdot \vec{I}_j \right], \quad (1.3)$$

and

$$H_Z = -\hbar \vec{B}_0 \cdot \sum_i \gamma_i \vec{I}_i, \quad (1.4)$$

where μ_0 is the permeability of free space, \hbar is the Planck constant, γ_i is the gyromagnetic ratio of the nuclear isotope, r_{ij} is the distance between the spins, k_F is the Fermi wave-number, and the \vec{I}_i 's are the nuclear spin operators. The relative magnitude of the RK and dipolar interactions is characterized by the parameter η . As the noble metals all have a face-centered-cubic structure, one can take the Fermi surface to be spherical. This approximation gives

$$f(2k_F r_{ij}) = \cos(2k_F r_{ij}) - \sin(2k_F r_{ij}) / (2k_F r_{ij}). \quad (1.5)$$

for the distance dependence of the interaction between nuclear spins. The oscillatory behavior of the RK interaction can lead to ferromagnetic or antiferromagnetic interactions between the nuclear spins. The cubic symmetry of the lattice excludes any electric quadrupolar (or higher order) interactions between the moments and electric field gradients in the system [6].

Table 1.1: Nuclear magnetic properties of the noble metals.

Isotope	μ (μ_n)	$\gamma/2\pi$ (kHz/mT)	κ (K-s)	T_2 (ms)
^{197}Au	0.143	0.741	4.6	2
^{107}Ag	-0.113	1.812	12	10
^{109}Ag	-0.130	2.084	9	10
^{63}Cu	2.22	11.55	1.27	0.15
^{65}Cu	2.38	12.38	1.09	0.15

In Table 1.1 are listed several of the relevant physical properties [7] of the noble metals: the magnet moment μ , the gyromagnetic ratio $\gamma/(2\pi)$, the Korringa constant κ , and the spin-spin relaxation time T_2 .

1.2 Nuclear Magnetic Ordering in Metals

When the nuclear spin temperature is on the order of the interaction energy of the spins, it is possible for the moments to become magnetically ordered. The phase diagram in copper [2] and silver [8, 9] has been studied at positive temperatures, where the competition between the anisotropic dipolar interaction and the RK interaction lead to a rich set of ordered structures [10]. The transition temperature for copper is found to be 56 nK [11], while for silver it is 560 pK [12]. Experimentally, it is found that silver is an antiferromagnetic exchange dominated system [3], while in copper the nuclear spin interaction is dominated by the anisotropic dipolar interaction [1].

At constant positive temperatures, the ordered arrangement of the nuclear spins is determined by minimizing the Helmholtz free energy,

$$F = U - TS, \quad (1.6)$$

where U is the internal energy of the system, T the temperature, and S the entropy.

At negative temperatures, the situation takes a peculiar turn. The stability criterion for the Helmholtz free energy now leads to the system *maximizing* its free energy. This can be seen by considering the thermodynamic stability of the system shown in

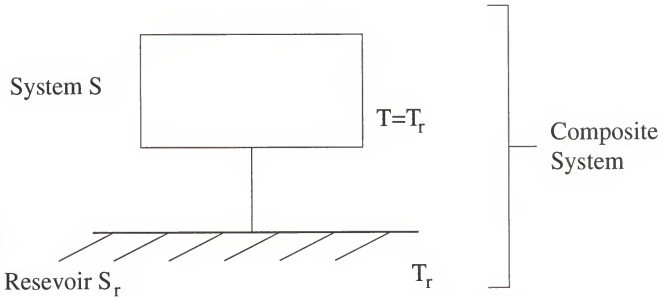


Figure 1.1: The composite system which is described in the text.

Figure 1.1. The composite system consists of a large thermal reservoir, and the system of interest, between which only heat can be exchanged. The reservoir is simply a conceptual tool introduced to hold the temperature constant. The total entropy of the system is $S_{total} = S_r + S$, where S_r is the entropy of the reservoir, and S is the entropy of the system. The temperature T of the system is the same as that of the reservoir, which is at T_r . At positive temperatures, the equilibrium of the composite system is characterized by

$$d(U + U_r) = 0, \text{ and} \quad (1.7)$$

$$d^2(U + U_r) > 0, \quad (1.8)$$

given that $dS_{total} = 0$, which implies $dS_r = -dS$. A change dS_r in the entropy of the reservoir results in an energy change $dU_r = T_r dS_r$. This leads to

$$\begin{aligned} d(U + U_r) &= 0, \\ &= dU + T_r dS_r, \end{aligned} \quad (1.9)$$

$$= dU + T (-dS), \quad (1.10)$$

$$= d(U - TS), \quad (1.11)$$

so that the Helmholtz free energy $F = U - TS$ of the system is an extremal. To determine if it is a minimum or maximum, first consider $d^2(U + U_r)$. One finds that

$$d^2U_r = \frac{\partial^2 U_r}{\partial S_r^2} (dS_r)^2, \quad (1.12)$$

$$= \frac{\partial T_r}{\partial S_r} (dS_r)^2, \quad (1.13)$$

$$= 0,$$

as the reservoir temperature T_r is constant. This leads to $d^2(U + U_r) = d^2U$, which is greater than zero, and so U is minimized. The condition on the free energy now takes the form

$$d^2F = d^2(U - TS), \quad (1.14)$$

$$= d^2U - T d^2S. \quad (1.15)$$

The differential d^2S is zero since S is the independent variable whose deviation from equilibrium is being considered. This leads to

$$d^2F = d^2U, \quad (1.16)$$

so that d^2F is greater than zero, as d^2U is greater than zero. This implies that F is a local minimum. For the negative temperature case, the equilibrium conditions are set by

$$d(U + U_r) = 0 \quad (1.17)$$

and

$$d^2(U + U_r) < 0, \quad (1.18)$$

at constant S_{total} . This leads, according to the above, to the free energy F being a local maximum.

However, this argument concerning the free energy of the nuclear spin system is not quite complete. Based on the above, one might say that if antiferromagnetic

(ferromagnetic) order is achieved at positive spin temperatures, then ferromagnetic (antiferromagnetic) order is the natural result to expect for ordering at negative temperatures. This holds true only for short range nearest-neighbor interactions [13, 14]. The long range dipolar interaction leads to the possibility of having both antiferromagnetic or ferromagnetic ordering at opposite signs of temperature. This has been demonstrated in work on the insulators CaF_2 and LiF by Abragam and co-workers [13]. In this case, the negative temperatures were achieved in the rotating frame, where the nuclear spin order was transferred from the Zeeman to the secular part of the dipolar Hamiltonian.

Another way to see that the situation is not straightforward is to consider the interactions in the ordered state at positive and negative temperatures. The ordered state at negative temperatures is identical to the ordered state at positive temperatures of the system in which the signs of all the interactions have been flipped. Therefore, if a system orders ferromagnetically at positive temperatures, it must order antiferromagnetically at negative temperatures, but an antiferromagnet at positive temperatures can be an antiferromagnet at negative temperatures.

A phase diagram for the ordered state of silver nuclear spins at negative temperatures has been determined experimentally by Hakonen and co-workers [15]. The dashed line in Figure 1.2 represents a theoretical phase boundary for negative temperatures, and the solid line is the phase boundary determined from [8] for the antiferromagnetically ordered state at positive temperatures. The two filled circles are the basis of the negative temperature phase boundary they have constructed. However, the paucity of data makes the phase diagram speculative, at best. From their data, they estimate the critical polarization in zero field and $5 \mu\text{T}$ to be $p_{\text{crit}} = -0.49$, which corresponds to a critical entropy of $S_{\text{crit}}/R \ln 2 = 0.82$. The two data points are obtained from the static susceptibility $\chi'(0)$ shown in Figure 1.3, taken in zero magnetic field (\circ), and at $5 \mu\text{T}$ parallel (\times) and perpendicular (∇) to the sample

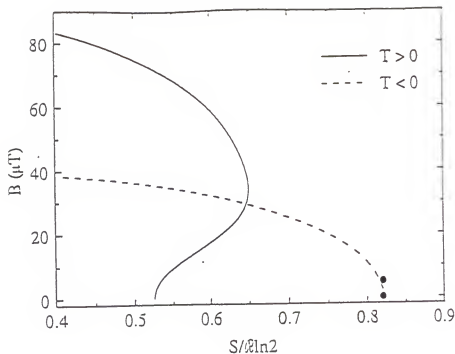


Figure 1.2: Phase diagram from reference [14], as described in the text.

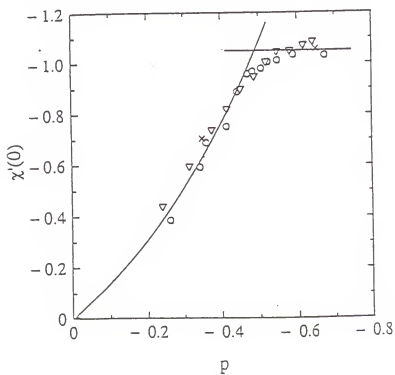


Figure 1.3: Static magnetic susceptibility in zero field and $5 \mu T$ as a function of spin polarization, from reference [14].

foils. The static susceptibility is calculated from the absorption signal $\chi''(f)$ using the Kramers-Kroönig relation $\chi'(0) = (2/\pi) \int_0^\infty (\chi''(f)/f) df$.

The polarization scale p in Figure 1.3 deserves some comment, as it is not a meaningful quantity in the ordered state, or in zero field. The polarization of the nuclear spins is actually determined at a ‘high’ magnetic field of 200 μT , using the formula [13] $p = A \int \chi''(f) df$ (the proportionality constant A is fixed by spectra taken at approximately 1 mK). The magnetic field is then adiabatically reduced to its final zero (or low) field value. Instead of the polarization, the horizontal axis should be the entropy of the nuclear spins, which is well defined in the ordered and paramagnetic state. For non-interacting spin 1/2 moments, this has a simple relation to the absolute value of the polarization $|p|$, given by

$$S/R = \ln 2 - 1/2((1 + |p|) \ln(1 + |p|) + (1 - |p|) \ln(1 - |p|)). \quad (1.19)$$

Another point is the comparison of the parameters determined from the Curie-Weiss law

$$\chi'(0) = \frac{C}{T - \Theta}, \quad (1.20)$$

where C is the Curie constant, and Θ is the Curie-Weiss temperature. Hakonen and coworkers found $\Theta = -4.8$ nK at positive temperatures, and $\Theta = -2.8$ nK at negative temperatures. Within the mean field theory, it has been shown [14] that one finds the same Θ for both signs of temperature. This result is in agreement with the nuclear susceptibility measurements on rhodium [16], where the Curie-Weiss temperature was found to be the same at positive and negative temperatures. The questions regarding the work on silver by Hakonen and co-workers prompted us to begin studying this system, to see if a consistent picture could be developed.

1.3 Negative Spin Temperatures

There are several techniques that have been used to generate negative temperatures in nuclear spin systems. In normal NMR, this is typically done with a 180 degree pulse. At the Larmor frequency γB_0 (where B_0 is the static field), the excitation B_{exc} is applied for a time t such that the precession angle θ satisfies $\theta = \gamma B_{exc} t = \pi$.

Another well known technique is that of adiabatic fast passage [17]. A magnetic field B of fixed magnitude but of variable direction is applied to the magnetic moments. The magnetization M is initially parallel to B . The changing direction of the field can be described by an angular velocity ω . If the condition

$$\gamma B \gg \omega \quad (1.21)$$

holds, then the magnetization M will stay aligned with the field B , even as it moves.

This can be exploited directly in high frequency pulsed NMR experiments. A rotating field B_1 of frequency ω is applied perpendicular to the static field B . When off-resonance, the magnetization M is almost completely parallel to the effective field $B_{eff} = \sqrt{B_1^2 + [\omega/\gamma - B_0]^2}$ in the rotating frame. By sweeping the excitation frequency through the resonance slowly, the magnetization M will follow B_{eff} in the rotating frame. At resonance, the magnetization is aligned with B_1 . By continuing the frequency sweep through the resonance, the magnetization will end up in the opposite direction of the static field. The only caveat is that the spin-lattice relaxation time (T_1) must be longer than the time it takes to make the frequency sweep.

An interesting technique was used by Purcell and Pound [18] in their pioneering work. They removed a LiF sample from a large static field and placed it in a small solenoid parallel to a field of ~ 100 gauss. They then discharged a capacitor through the solenoid so that the direction of the field was reversed to ~ -100 gauss, and returned the sample to the large static field (the entire process took approximately

3 seconds). They found the resulting magnetization to be reversed, indicating that the moments were now at negative temperatures.

This technique was refined by Oja and co-workers [19], and has subsequently been used as the chief means of generating negative spin temperatures in metals. It has been employed by Hakonen and co-workers in their work on silver [12] and rhodium [16]. The static field is flipped on a very short time scale compared to T_2 , the spin-spin relaxation time, so that the moments do not follow the direction of field. In Figure 1.4, the upper part of the diagram shows the situation before the field is inverted, and the lower part shows the final result. For silver, $T_2 \sim 10$ ms, and in rhodium, $T_2 \sim 10.5$ ms. The best inversion efficiency in silver was 90% at polarizations of $\sim 30\%$, while at higher polarizations (60-70%), the efficiency dropped to ~ 60 -70%. In rhodium, for polarizations less than 40%, inversion efficiencies as high as 95% could be achieved. However, at higher polarizations, the inversion efficiency again dropped below 60%.

A more 'sophisticated' way to flip the spins is by using a suitable square wave pulse. This is essentially a single-period version of the 180 degree pulse, and was first described by Friedmann, et al. [20] in their work on ^3He . The method illustrates why the pulse frequency has to increase as the pulse duration is reduced to one or two periods of oscillation. This technique was also tried in the rhodium work, but efficiencies of only 60% could be achieved, even at low polarizations [16].

While there are several techniques available to invert the nuclear magnetization in metals, none of them are very satisfactory from a practical standpoint. Neither the conventional 180 degree pulse nor the adiabatic fast passage is useful for bulk metals at very low temperatures. They require high frequencies, which leads to the skin effect, and the RF field B_{exc} heats up the conduction electrons, causing the nuclear spins to relax. The inversion schemes discussed here are not well characterized, and their failings at high polarization are not understood. The inability to attain high

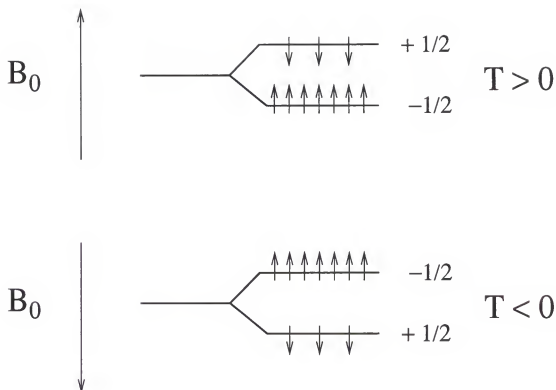


Figure 1.4: Schematic representation of the field inversion technique. Note that the gyromagnetic ratio in silver is negative. Therefore, the spin is anti-parallel to the magnetic moments, which are depicted with arrows.

negative polarizations using present techniques limits the work that can be done on nuclear spin systems in the ordered state at negative temperatures. This has led us to develop a new technique for inverting the nuclear magnetization. The physical model and experimental work characterizing this new scheme are discussed in Chapter 3. These results should prove useful to workers in the low temperature field of nuclear magnetism in metals. In Chapter 2, the cryogenic apparatus and electronics used in this work are described. Chapter 4 has some suggestions for future work. Appendix 1 presents the results of measurements on the nuclear susceptibility of PrBe_{13} , and the observation of nuclear antiferromagnetic ordering in this system.

CHAPTER 2

EXPERIMENTAL DESIGN AND TECHNIQUES

To cool the silver nuclei to ultra-low spin temperatures, the silver sample was used as the second stage of a two-stage nuclear demagnetization cryostat. In the first part of this chapter, the cryogenic apparatus used to obtain these temperatures is described. The second section covers the electronics and design of the silver experiment. The third section describes the thermometry used to monitor the performance of the cryostat. The final section discusses the experimental procedures used in the experiment.

2.1 Cryostat

The cryostat is suspended from a triangular aluminum table that rests on three Vibraplane¹ air isolation pistons. The pistons are anchored to a concrete tripod whose legs are isolated from the building foundation and rest on 2 ton concrete pads. The pads serve as a first stage in de-coupling the cryostat from building vibrations. By pressurizing the pistons with N₂ from a high pressure gas cylinder, one effectively floats the table and mechanically isolates the cryostat from the tripod. In this way, coupling of the refrigerator to building vibrations is further minimized.

Special care has gone into providing RF shielding of the cryostat in order to minimize noise-induced heating. A large screened room encloses the upper part of the cryostat. In this room are kept all of the sensitive electronics that are essential to running experiments and the cryostat. Computers are connected to the equipment

¹Kinetic Systems, Boston, MA 02131.

in the room via optical cables that are fed through a small pipe in the roof of the shielded room. The lower part of the cryostat is housed in a large aluminum can that is bolted to the floor of the shielded room.

2.1.1 Dilution Refrigerator

The cryostat used in this work consists of two principle cooling stages: a commercial dilution refrigerator unit and a copper nuclear demagnetization stage.

The dilution refrigerator is an Oxford Instruments² 1000. Dilution refrigerators have been in use now for a number of years, and the general principles governing their operation are well documented [21, 22], so only those aspects key to this work will be described. A more thorough description of the cryostat can be found in [23, 24, 25].

The lowest operating temperature of the dilution unit is ~ 4.5 mK at low circulation rates (~ 0.35 mmol/s of ^3He). This base temperature is typical of modern dilution refrigerators. However, the real figure of merit for such machines is their cooling power. In Figure 2.1, the cooling power as a function of temperature is plotted for a fixed ^3He circulation rate of $\dot{n} = 1.27$ mmol/s. The fit is according to the model described in [26]. The functional form of the cooling power can be written as

$$\frac{dQ}{dt} = aT^2 - b, \quad (2.1)$$

where a and b are fitting parameters. The parameter b represents the residual heat leak to the fridge at this circulation rate, and is found to be $1.7 \mu\text{W}$. The circulation rate of $\dot{n} = 1.27$ mmol/s is found to be the most efficient for pre-cooling the nuclear demagnetization stage. This upper limit for the pre-cooling efficiency occurs because one begins to circulate appreciable amounts of ^4He above this point, while the ^3He circulation rate becomes saturated.

²Oxford Instruments, 130A Baker Avenue, Concord, MA 01742, phone: (508) 369-9933.

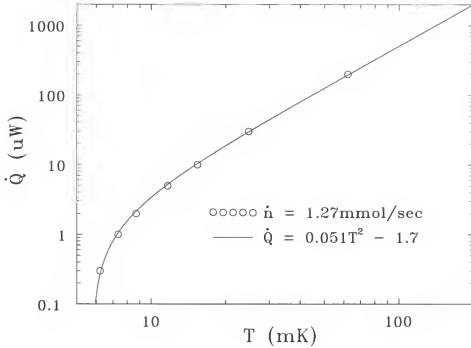


Figure 2.1: Cooling power of the dilution refrigerator.

The thermal link between the dilution refrigerator and copper nuclear demagnetization stage is made with an aluminum superconducting heat switch [27]. The superconducting transition temperature for aluminum in zero magnetic field is $T_c(B=0) \sim 1.2 \text{ K}$, while the critical magnetic field at 0 K is $B_c(T=0) \sim 11 \text{ mT}$. For temperatures sufficiently lower than the transition temperature and in zero applied field, the switch is thermally insulating. The application of a field greater than B_c drives the aluminum into the normal state, where the thermal conductivity due to the conduction electrons recovers its linear temperature dependence.

2.1.2 Copper Nuclear Demagnetization Stage

The demagnetization stage consists of nineteen copper sheets, each a quarter-inch thick and 36 inches long. The width of each plate is such that when stacked together, they form a cylinder 2.5 inches in diameter. The top part of the plates is electron-beam welded to a large gold-plated copper flange 4.5 inches in diameter, which is

bolted into a copper cage. The cage is designed to provide space for experiments and thermometers to be attached to the top of the copper bundle, while providing a convenient way to connect the bundle to the bottom of the aluminum heat switch.

The bottom of the copper bundle ends in a small flange to which the silver experiment is bolted. The copper flange has been gold-plated to prevent oxidation. In Figure 2.2, the copper-to-silver flange connection is shown in detail. Eight 3/4 inch 6-32 Be-Cu screws are used to hold the flanges together. To ensure good metallic contact at low temperatures, small tungsten washers (50 mils thick) were used to compensate for the thermal contraction of the connecting materials.

The end-compensated 8 T magnets that are used for adiabatic demagnetization of the copper bundle and silver experiment were made by Cryomagnetics³. The magnet used for the bundle has a current to field ratio $B/I = 0.0935$ T/A, while the second magnet for the silver experiment has a ratio of $B/I = 0.0976$ T/A. The field profile of the first magnet is such that the nuclear heat capacity of 350 moles of copper is equivalent to that of roughly 170 moles in the peak field region.

The magnets were energized to 75 amps by a 100 amp Kepco ATE6-100A power supply⁴. For currents less than 10 amps, a smaller Kepco ATE 6-10M unit was used. Both power supplies were operated by computer controlled DC voltage ramps built by the physics department electronics shop. Details on the demagnetization procedure are deferred to chapter 3, where experimental procedures are discussed.

2.2 Silver Stage

The silver experiment is in essence a scaled down version of the copper stage. It forms a second demagnetization stage that is pre-cooled by the copper bundle to 100 μ K in 7 T. In Figure 2.2, the main components of the silver stage are shown. The

³Cryomagnetics, Inc., 739 Emory Valley Road, Oak Ridge, TN 37831-0548, phone: (615) 482-9551.

⁴Kepco, Inc., 131-38 Sanford Avenue, Flushing, NY 11352, phone: (718) 461-7000.

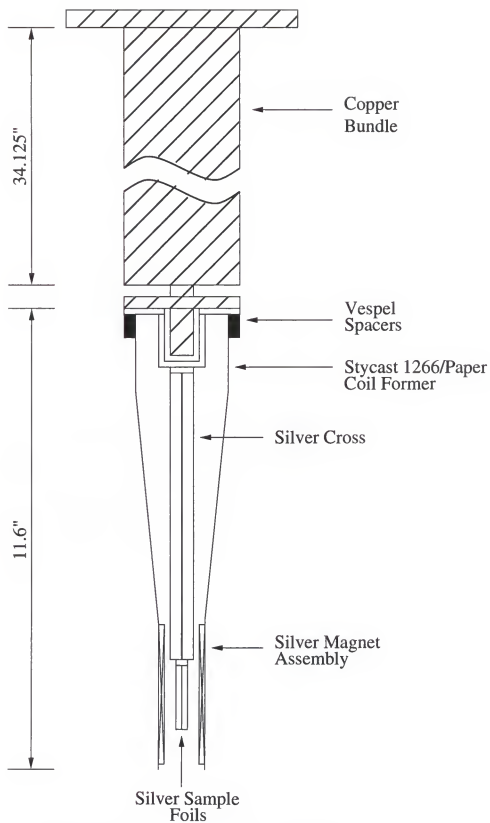


Figure 2.2: Silver cross and sample geometry.

Table 2.1: Annealing results for silver foils.

RUN	T (°C)	P _{O₂} (Torr)	time (hours)	RRR	Comments
1	650	10 ⁻⁴	5	400	turn off O ₂ at 650 °C
2	700	2 · 10 ⁻⁴	4	470	turn off O ₂ at 700 °C
3	750	10 ⁻⁴	3	480	turn off O ₂ at 750 °C
4	800	10 ⁻⁴	1.7	460	turn off O ₂ at 800 °C
5	800	10 ⁻⁴	2.5	675	turn off O ₂ at room temperature
6	800	10 ⁻⁴	2.5	560	turn off O ₂ at 300 °C

silver flange bolted to the bottom of the copper stage is made of 5 9's purity silver plate. To this are TIG-welded⁵ a symmetric pair of silver stand-offs that clear the copper button that protrudes from the bottom flange of the copper stage. The silver cross is TIG-welded to these standoffs. The cross was machined from a 5 9's purity Marz grade silver rod from MRC⁶. The cross design minimizes the amount of silver that can give rise to eddy-current heating during the demagnetization of the sample. It also provides excellent rigidity, thereby reducing heating due to vibrations. The silver flange and cross were annealed for 10 hours at 750 °C under an oxygen pressure of $3 \cdot 10^{-4}$ torr. From previous work annealing silver, the residual resistivity ratio (RRR) of the components is estimated to be > 550 .

The bottom of the silver cross ends in a small cup into which the sample has been welded with an acetylene torch. The silver sample consists of a stack of 16 silver foils $3 \text{ mm} \times 50 \text{ mm} \times 0.1 \text{ mm}$. These were cut from a $100 \text{ mm} \times 100 \text{ mm} \times 0.1 \text{ mm}$ Puratronic grade (5 9's pure) silver foil from Alpha-Aesar⁷. To avoid adding any iron impurities to the sample, a pair of ceramic scissors from Kyocera⁸ were used to cut the foils to the proper dimensions. As silver has a high vapor pressure at elevated

⁵Tungsten Inert Gas

⁶Materials Research Corporation, 560 Route 303 South, Orangeburg, NY 10962, phone: 914-359-4200.

⁷Aesar, 892 Lafayette Rd., Seabrook, NY 03874-1087.

⁸Kyocera America, Inc. 8611 Balboz Avenue, San Diego, CA 92123.

temperatures, some tests were run to determine the optimum annealing procedure in order to minimize sample loss during heat treatment. Table 2.1 summarizes the results of this work. The goal was to maximize the residual resistivity ratio while minimizing the annealing time to cut down sample loss. The sample was annealed using the parameters from run 5.

To minimize the effects of stray magnetic fields on the experiment, the cold plate radiation shield of the dilution refrigerator was modified to seat two high permeability cylinders centered on the silver sample. On the outside is fitted one of mu-metal (0.1 in wall thickness, 7 in long, 3.8 in o.d.) and on the inside of the shield is one of Cryoperm⁹ 10 (0.12 in wall thickness, 5 in long, 3.63 in o.d.). To keep the permeability of the material high at low temperatures, the Cryoperm was annealed in ≥ 1 atmosphere of ⁴He according to the following recipe [22]: 1) 2 hours at 1100 °C, 2) cool to 500 °C in 3 hours, 3) cool to room temperature in 12 hours, 3) anneal for 30 minutes at 550 °C, 4) cool to 470 °C in 40 minutes, 5) anneal for 2 hours at 470 °C, 6) cool to room temperature in 2.5 hours.

2.3 NMR Coils and Electronics

Continuous Wave (CW) SQUID¹⁰ NMR was used to measure the magnetic susceptibility of the silver nuclear spins. The detection system consisted of two sets of orthogonal coils as shown in Figure 2.3. However, the first RF SQUID¹¹ detector that was connected to the vertical pick-up coil never worked properly. All of the measurements reported in this work are for a configuration with the second RF SQUID connected to the horizontal pick-up coil, with the vertical excitation and compensation coils, and the horizontal static field coil. Coil parameters are listed in Table 2.2.

⁹Vakuumschmelze, D-6450, Hanau, Germany.

¹⁰Superconducting QUantum Interference Device.

¹¹S.H.E Corporation, 4174 Sorrento Valley Blvd., San Diego, CA 92121.

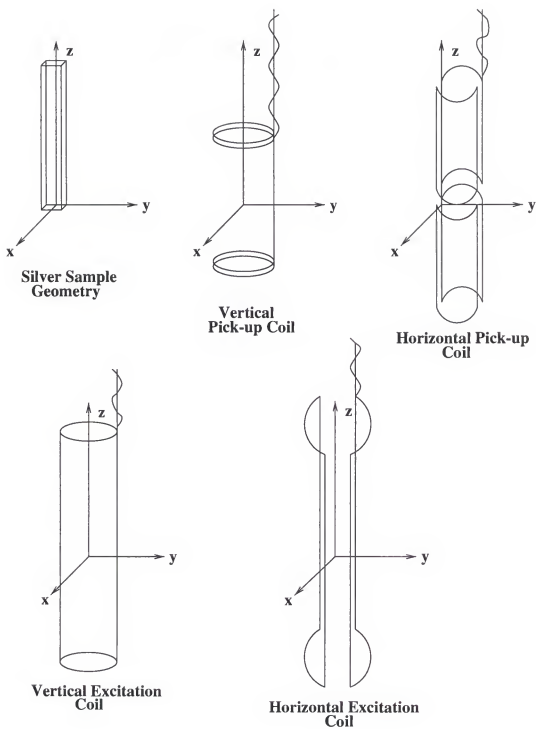


Figure 2.3: The relative orientation of the pick-up and excitation coils.

Table 2.2: Coil parameters

Design	Wire	B/I (mT/A)	L (μ H)	Type
Compensation \hat{z}	4 mil Cu	1.3	—	Solenoid
Compensation \hat{x}	4 mil Cu	1.4	—	Helmholtz
Excitation \hat{z}	4 mil Cu	8.4	—	Solenoid
Excitation \hat{y}	4 mil Cu	3.6	—	Helmholtz
Static Field \hat{z}	2 mil Niomax	40	—	Solenoid
Static Field \hat{y}	2 mil Niomax	3.55	—	Helmholtz
Pick-up \hat{x}	2 mil Niomax	—	2.1	Astatic Helmholtz pair
Pick-up \hat{z}	2 mil Niomax	—	1.98	Astatic solenoid pair

The typical experimental arrangement is shown in Figure 2.4. An SRS¹² DS340 Digital Signal Generator is used to feed both the excitation and compensation coils. The resistors make the DS340 perform as a current source, and the ratio of the resistor values is chosen to balance out as much of the background signal as possible. The inverter in the compensation line is necessary to adjust the relative phase of the two signals in order to reduce the background. The pick-up coils form a superconducting loop that is flux-linked to the RF SQUID sensor. The SQUID is operated in the slow flux-locked-loop mode, corresponding to a maximum slew rate of $1.3 \times 10^3 \phi_0$ sec, where ϕ_0 is the flux quantum. The feedback signal from the SQUID electronics is fed into an Ithaco¹³ 393 lock-in that uses the SYNC signal from the DS340 frequency generator as its reference input. The time constant setting of the lock-in is 1.25 seconds and the sensitivity is 3 mV. The in-phase and quadrature voltage signals from the lock-in were measured by Hewlett-Packard 34401A and 34574 digital voltmeters (DVM). A PC outside of the shielded room using LabWindows¹⁴ and a IEEE 488 card¹⁵ is connected to the DVM's and signal generator via an HP-IB optical extender.

¹²Stanford Research Systems, Sunnyvale, CA 94089.

¹³Ithaco, Inc. 735 W. Clinton St., Ithaca, NY 14850.

¹⁴National Instruments, 6504 Bridge Point Parkway, Austin, TX 78730.

¹⁵*ibid.*

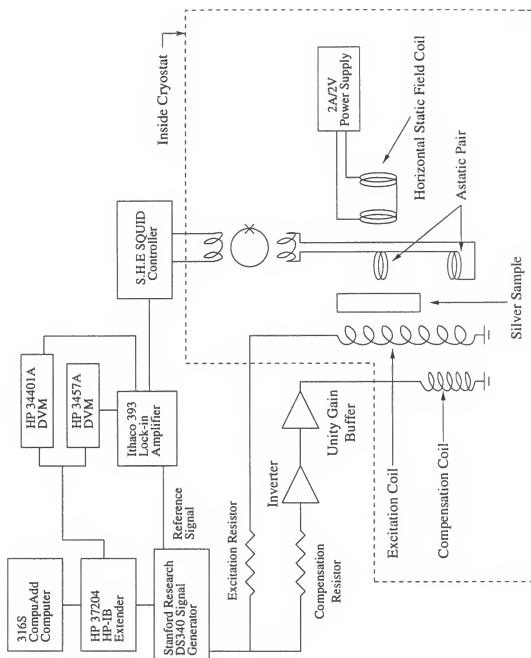


Figure 2.4: Electronic circuit for the silver experiment.

A program written in the LabWindows environment controlled the frequency and amplitude of the signal generator while recording the DVM readings.

2.3.1 Spin-flip Electronics

To invert the silver nuclear moments, a large sinusoidal pulse (comparable to the static field) is sent into the excitation coil. The pulses are generated with the Arbitrary Waveform Composer software that comes with the Stanford Research DS345 Digital Signal Generator. A PC dedicated to running this software package is connected to the DS345 via another HP-IB optical extender. Once the desired waveform has been generated, it is loaded into the DS345's memory, and the signal generator used for frequency sweeps is disconnected from the excitation and compensation coils. The 'tipping' generator is then connected to the excitation coil through a 51 Ω resistance, and the tipping pulse is triggered from the front panel of the DS345. The tipping generator is then disconnected, and the signal generator for frequency sweeping is re-connected to the compensation and excitation coils.

2.4 Thermometry

The temperature of the copper nuclear demagnetization stage is monitored by two thermometers. A ^3He melting curve thermometer (MCT) is used for temperatures above 1 mK, while a platinum (Pt) NMR thermometer is used for lower temperatures.

2.4.1 Melting Curve Thermometer

The melting pressure cell is a Straty-Adams strain gauge [28] that forms one of the low temperature arms of a capacitance bridge. The electronic configuration of the thermometer is shown in Figure 2.5.

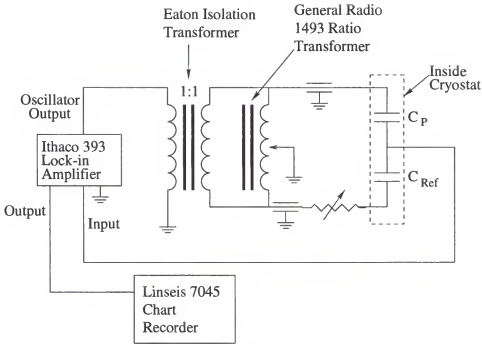


Figure 2.5: Electronic circuit for the melting curve thermometer.

The MCT is used as a self-calibrating primary thermometer, and is operated in zero magnetic field. The fixed points used to calibrate the thermometer are the superfluid A-phase transition ($T_A = 2.505$ mK) [29] in liquid ^3He and the Neel transition ($T_N = 0.934$ mK) [29] in the solid.

The strain gauge is driven by the internal oscillator of an Ithaco 393 lock-in amplifier at a frequency of 1.1 kHz, with an amplitude of $1.22 V_{rms}$. An Eaton¹⁶ one-to-one isolation transformer is used to separate the bridge from power ground. A General Radio 1493 ratio transformer is used to balance the bridge, and the ratio reading is converted to temperature based on a capacitance vs. pressure calibration taken at ~ 1 K. The small off-balance bridge voltage is fed to the lock-in, and the resulting DC output is sent to a chart recorder. For details on the design and operation of these strain gauges, the curious reader is directed to the review article by Adams[30].

¹⁶Eaton Corporation, Electronic Instrumentation Division, 5340 Alla Road, Los Angeles, CA 90066, phone: (213) 822-3061.

2.4.2 Pt NMR Thermometer

The Pt thermometer is used to measure the temperature of the copper bundle below the Neel transition of the ^3He solid, where the slope of the melting curve tends to zero. This thermometer has no fixed points, and so operates as a secondary thermometer calibrated against the MCT between T_N and ~ 10 mK. It relies on the Curie law susceptibility of the ^{195}Pt spins, and can be used to measured temperatures on the order of several μK .

A commercial PLM-3¹⁷ unit was used to perform NMR on the Pt sample. The layout of the thermometer and electronics is shown in Figure 2.6. The cable capacitance of the coax in the cryostat plus a 1 foot section of BNC cable at room temperature gives a capacitance to ground of 228 pF. The NMR coil that completes the tank circuit was wound with 3 mil copper wire and has an inductance of 5.9 mH. The tuning capacitor in the preamp is used to set the resonant frequency to 125 kHz. When tuned, the tank circuit has a quality factor (Q) ~ 8 . The static field coil to fix the Larmor frequency of the Pt nuclear spins is made from 9 mil Formvar insulated copper clad Supercon¹⁸ superconducting wire. The magnet consists of 10 full layers on a cylindrical copper former with two four layer, 0.32 inch long end correction windings. A minimal amount of Stycast 1266 epoxy was used to hold the wires in place. The magnet sits inside a copper tube whose outer surface has been coated with Pb, which is superconducting below 11 K. The entire magnet assembly is thermally anchored to the mixing chamber, and thermally isolated from the copper bundle by four 0.25 in diameter \times 0.4 in long rock maple [31] stand-offs. The current to fix the Larmor frequency at 125 kHz in the static field coil is 1.26 A.

It was found that the measured free-induction decay time T_2^* for the Pt was only 0.6 ms, which compares unfavorably with the known spin-spin relaxation time

¹⁷RV-Elektronikka Oy, Veromiehentie 14, SF-01510 Vantaa, Finland.

¹⁸Supercon, Inc., 830 Boston Turnpike, Shrewsbury, MA 01545.

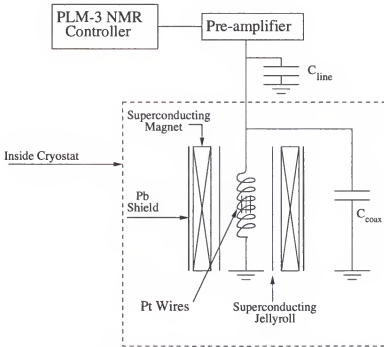


Figure 2.6: Schematic diagram of the Pt NMR circuit.

of $T_2 = 1.2$ ms [7]. This was attributed to field inhomogeneities in the magnet, which were reduced by inserting a superconducting ‘jellyroll’ inside the static field coil. This design has been developed by Hechtfisher [32], and exploits the boundary condition of the magnetic field at the surface of a flat superconductor to produce very homogeneous small fields. The jellyroll is made of a 3.5 inch \times 10 inch \times 2 mil sheet of NbTi from Teledyne Wah Chang¹⁹, and an insulating layer of 1 mil thick Mylar. The Mylar and NbTi are wound around a copper cylinder several times, and care is taken so that there are no superconducting shorts between the NbTi layers. Small amounts of Stycast 1266 and dental floss were used to hold the jellyroll on the former. After this was inserted into the bore of the static field coil, T_2^* was found to be ~ 1 ms.

The 500 Pt wires that form the NMR thermometer are in the form of a brush that is butt-welded to a small 5 9’s pure Pt plate. The Pt assembly was annealed in air for 3 hours at 900 °C. In order to avoid quartz contaminating the sample, the

¹⁹Teledyne Wah Chang, Albany, OR 97321.

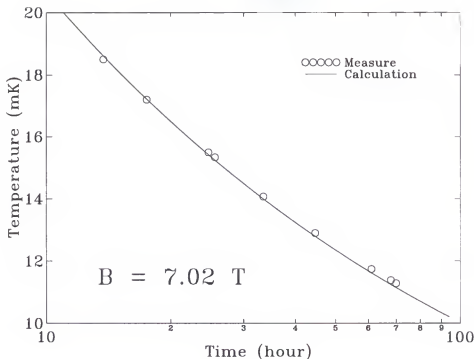


Figure 2.7: Temperature of the bundle during the precool.

Pt was placed in a small alumina²⁰ boat inside a quartz tube in the annealing oven. This recipe yielded RRR values of over 1000 on Pt test samples [33].

2.5 Experimental Procedures

A typical run to take NMR data on the silver experiment starts with precooling the copper bundle in a field of approximately 7 T for 3-4 days. This brings the temperature of the bundle to just over 11 mK, and the magnetic heat capacity of the copper nuclei is on the order of 200 J/K. The temperature of the bundle during this procedure is shown in Figure 2.7. The bundle is then demagnetized from these initial conditions according to the following recipe distilled from practical experience and computer simulations:

$$7 \text{ T} \xrightarrow{210\text{min}} 3.7 \text{ T} \xrightarrow{180\text{min}} 1.9 \text{ T} \xrightarrow{120\text{min}} 0.93 \text{ T}.$$

²⁰SGP, Willow Grove, PA 19090.

When the field of the magnet is ~ 3 T, the heat switch is opened (made superconducting) and the circulation rate of the dilution refrigerator is reduced to ~ 0.35 mmol/s. The magnet is persisted at 0.93 T in order to switch over from the 100 A to the 10 A Kepco power supply, which is then used to control the remainder of the demagnetization for the copper bundle with a higher precision.

The 100 A Kepco is now brought inside the RF shielded room and connected to the second magnet. The demag of the first magnet is continued with the 10 A supply to 0.37 T in 150 minutes, at which point the magnet is again put in persistent mode and a ^4He transfer is made. The second magnet is then energized to 6.7 T and persisted. The final stage of the bundle demagnetization is continued according to:

$$0.37 \text{ T} \xrightarrow{120\text{min}} 0.19 \text{ T} \xrightarrow{240\text{min}} 0.094 \text{ T} \xrightarrow{240\text{min}} 0.047 \text{ T}.$$

The copper bundle is now at $95 \mu\text{K}$. There is now a 12 hour wait as the silver nuclei come into thermal equilibrium with the copper stage and reach nearly 100% polarization.

For small polarization p , the relaxation of the silver nuclei is described by the well known rate equation

$$\frac{dp}{dt} = \frac{1}{T_1}(p_{eq} - p), \quad (2.2)$$

where T_1 is the nuclear spin-lattice relaxation time and p_{eq} corresponds to the equilibrium polarization. Using the Korringa relation $\kappa = T_1 T_{eq}$ [34], and the fact that for small polarization $p \propto 1/T$, the above equation can be re-written as

$$\frac{d}{dt}\left(\frac{1}{T_{eq}}\right) = \frac{T_{eq}}{\kappa}\left(\frac{1}{T_{eq}} - \frac{1}{T}\right), \quad (2.3)$$

where T_{eq} denotes the temperature to which the silver nuclear spins are relaxing. This is identified with the temperature of the silver conduction electrons, which are taken to be in equilibrium with the conduction electrons of the copper bundle.

For high polarization, the above rate equation no longer holds, and has to be modified [35, 36] to take into account the full relation of the polarization to the magnetic field B . The rate equation then becomes

$$\frac{dp}{dt} = \frac{\hbar\gamma B/2k_B}{\kappa} \left(\coth\left(\frac{x}{2}\right) - \coth\left(\frac{x_{eq}}{2}\right) \right) p, \quad (2.4)$$

where $x = \hbar\gamma B/k_B T$, $x_{eq} = \hbar\gamma B/k_B T_{eq}$, and I is the nuclear spin. The above equation can be simplified as the polarization for spin $I = 1/2$ is given by

$$p = \tanh\left(\frac{\hbar\gamma B}{2k_B T}\right). \quad (2.5)$$

Substituting this back into the rate equation yields

$$\frac{dp}{dt} = \frac{\hbar\gamma B/2k_B}{\kappa} \left(\frac{1}{p} - \frac{1}{p_{eq}} \right) p. \quad (2.6)$$

In Figure 2.8, the polarization as a function of time is shown for both the ^{107}Ag and ^{109}Ag nuclear spins (time zero corresponds to the demag of the copper bundle from 0.37 T). Twelve hours after the demagnetization of the copper bundle, the 1 K pot is closed and the magnet on the silver experiment is demagnetized from 6.7 T $\xrightarrow{120\text{min}}$ 0.04 T. At this point, a small 2-A/2-V power supply (powered by deep cycle marine batteries) is used to energize the small NMR static field coil to $\sim 90 \mu\text{T}$, and the current in the large second magnet is ramped to zero in 1 minute. The static field coil is then increased to $\sim 850 \mu\text{T}$. The large magnet is persisted, and the current leads from the 100 A Kepco are disconnected. The large magnet is now depersisted with the current leads open circuited for 1 minute, and then persisted. At this point, the flux-transformer heater for the SQUID is turned off, and hopefully everything is working. The data acquisition program is now initiated, and frequency sweeping begins.

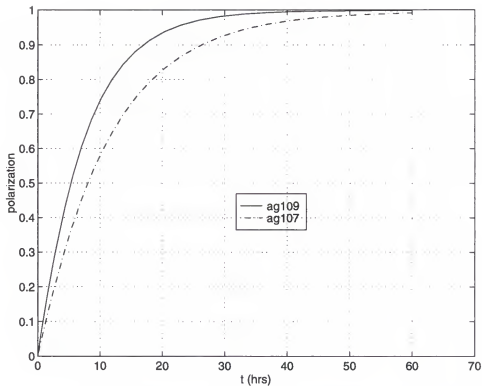


Figure 2.8: Predicted pre-cooling curve for the silver nuclei at 100 μ K in 6.7 T.

For the frequency sweeps, the excitation field B_{exc} is typically 5 nT, and the canonical frequency step is 2 Hz. The program has a user defined dwell time for each step, which is set to 2 or 3 seconds. Once the dwell time has been reached, the program queries the DVM's to obtain both channels of the lock-in output, and saves the information to a file. The program then steps the frequency to the next value. After acquiring the raw data, there is usually an appreciable amount of signal left. To eliminate this, a number of large tipping pulses are used to heat the spins until the magnetization is in the noise. At this point, frequency sweeps of the background signal are taken. Typically, four background sweeps are acquired for signal averaging. The excitation signal is now disconnected, and several sweeps with the compensation signal alone are taken. This gives a 'calibration' of the frequency dependence of the gain of the SQUID, as the compensation coil does not couple to the sample, but does

couple to the SQUID pick-up coil. Note that all of the data acquired is taken in the same static field, as the background has a large field dependence.

After the data taking is complete, the 1 K pot is opened (the maximum ‘hold’ time of the pot is ~ 7 hours). The flux-transformer heater is turned on, and the small static field coil is ramped to zero. The copper bundle is then remagnetized according to:

$$0.047 \text{ T} \xrightarrow{240\text{min}} 0.094 \text{ T} \xrightarrow{240\text{min}} 0.19 \text{ T} \xrightarrow{120\text{min}} 0.37 \text{ T}.$$

A helium transfer is made at the completion of the remagnetization, and the second magnet is energized to 6.7 T and persisted. The demag of the copper bundle is then carried out from 0.37 T as before, and the whole process cycles through. A single demagnetization of the large copper bundle is capable of precooling the silver stage 4-5 times in this fashion.

CHAPTER 3

THEORETICAL CONSIDERATIONS AND EXPERIMENTAL RESULTS

The steady-state response of the silver nuclei are modelled using the Bloch equations. The coupling of the two silver nuclear species via the RK interaction and the dipolar interaction for the sample foil geometry are included. Lineshapes for the sample are calculated for the particular excitation and pick-up coil assemblies used in this work. The theoretical description of the spin-flip dynamics is then described, and the last sections compare the experimental results with the models.

3.1 Modified Bloch Equation

The magnetic properties of nuclear moments are well described by the phenomenological equations of Bloch [37]. In the case of highly polarized silver, where there are two distinct magnetic nuclear species, the equations have to incorporate an extra term that describes the RK and dipolar coupling between the two. This term is defined as

$$R = \sum_i \frac{J_{ij}}{\mu_0 \rho \gamma^2 \hbar^2} \quad (3.1)$$

$$= \frac{\eta}{\mu_0 \rho \gamma^2 \hbar^2} \sum_i \frac{f(2k_F r_{ij})}{r_{ij}^3} \quad (3.2)$$

and is the dimensionless measure of the strength of the exchange interaction relative to the averaged dipolar interaction. Here J_{ij} is the strength of the exchange interaction, and ρ is the number density of silver atoms. The equations of motion for the ^{107}Ag

and ^{109}Ag magnetizations now take the form (ignoring relaxation terms for simplicity)

$$\frac{d\vec{M}_{107}}{dt} = \gamma_{107}\vec{M}_{107} \times \left[\vec{B}_0 + \vec{B}_{exc} + (R + 1/3)\mu_0\vec{M}_{109} + \overset{\leftrightarrow}{D}\mu_0(\vec{M}_{107} + \vec{M}_{109}) \right] \quad (3.3)$$

and

$$\frac{d\vec{M}_{109}}{dt} = \gamma_{109}\vec{M}_{109} \times \left[\vec{B}_0 + \vec{B}_{exc} + (R + 1/3)\mu_0\vec{M}_{107} + \overset{\leftrightarrow}{D}\mu_0(\vec{M}_{107} + \vec{M}_{109}) \right], \quad (3.4)$$

where $\overset{\leftrightarrow}{D}$ is the shape-dependent demagnetization factor [17], the $1/3$ arises due to the Lorentzian field, and \vec{B}_0 and \vec{B}_{exc} are the static and excitation fields, respectively. This form of the Bloch equations was first used by Ekstrom and coworkers in their work on copper [1].

The outline of the calculations will be for a sample with cylindrical geometry, as this is analytically easier to handle, and the physical meaning of the results is clearer. The modifications of the solutions to the experimental foil geometry will be described at the end.

3.1.1 Steady-State Solutions for the Wire Geometry

For the wire geometry, the demagnetization factor is diagonal, and has $D_{xx} = D_{yy} = -1/2$ and $D_{zz} = 0$. The linear excitation field B_{exc} is decomposed into counter-rotating fields, and the only significant response will be from the counter-clockwise component $\vec{B}_{exc} = B_1(\cos(\omega t), -\sin(\omega t), 0)$.

The condition for steady-state precessions is given by approximating the \hat{z} -component of the ^{107}Ag and ^{109}Ag magnetizations with their respective equilibrium values, so that $M_z^{107} \approx M_0^{107}$ and $M_z^{109} \approx M_0^{109}$. For ease of calculation, complex, instead of vector notation, is now used. The excitation field now takes the form $B_{exc}^+ = B_1 \exp(j\omega t)$. The precessing magnetizations are given by $M_+^{107} = m^{107} \exp(j\omega t)$ and $M_+^{109} = m^{109} \exp(j\omega t)$, where $M_+^{107,109} = M_x^{107,109} + jM_y^{107,109}$.

The equations of motion now take the form

$$\begin{aligned} j\omega m^{107} = & -jm^{107}\gamma_{107}\left[B_0 + (R + 1/3)\mu_0 M_0^{109} + (1/2)\mu_0 M_0^{107}\right] \\ & + jm^{109}\gamma_{107}(R - 1/6)\mu_0 M_0^{107} + jM_0^{107}\gamma_{107}B_1 \end{aligned} \quad (3.5)$$

$$\begin{aligned} j\omega m^{109} = & -jm^{109}\gamma_{109}\left[B_0 + (R + 1/3)\mu_0 M_0^{107} + (1/2)\mu_0 M_0^{109}\right] \\ & + jm^{107}\gamma_{109}(R - 1/6)\mu_0 M_0^{109} + jM_0^{109}\gamma_{109}B_1. \end{aligned} \quad (3.6)$$

From this system of equations, one finds eigenfrequencies

$$\omega_{\pm} = \frac{1}{2} \left[\omega'_{107} + \omega'_{109} \pm \sqrt{(\omega'_{109} - \omega'_{107})^2 + 4\gamma_{107}\gamma_{109}(R - 1/6)^2\mu_0^2 M_0^{107} M_0^{109}} \right], \quad (3.7)$$

where

$$\omega'_{107} = \gamma_{107} \left[B_0 + (R + 1/3)\mu_0 M_0^{109} + (1/2)\mu_0 M_0^{107} \right] \quad (3.8)$$

and

$$\omega'_{109} = \gamma_{109} \left[B_0 + (R + 1/3)\mu_0 M_0^{107} + (1/2)\mu_0 M_0^{109} \right]. \quad (3.9)$$

To first order, the resonance frequencies are modified in two ways. In silver, $R \sim -2.5$ [3], so that the term $(R + 1/3)\mu_0 M_0$ corresponds to an overall downshift due to the antiferromagnetic exchange between the *unlike* nuclear spin species. The last term, $(1/2)\mu_0 M_0$ gives an upshift to the spins due to the torque of the precessing demagnetization field of the *same* spin species. This is illustrated by the data in Figure 3.1.

To higher orders, there is an overall repulsion term $4\gamma_{107}\gamma_{109}(R - 1/6)^2\mu_0^2 M_0^{107} M_0^{109}$ that represents the coupling between the precessing ^{107}Ag and ^{109}Ag magnetizations. This term scales as $(R - 1/6)^2 M_0^{107} M_0^{109}$. When the polarization p of the ^{107}Ag and ^{109}Ag spins are the same, this term becomes proportional to $(R - 1/6)^2 p^2$, the square of the polarization p , as $M_0 \propto p$. So for small polarizations, it is essentially negligible.

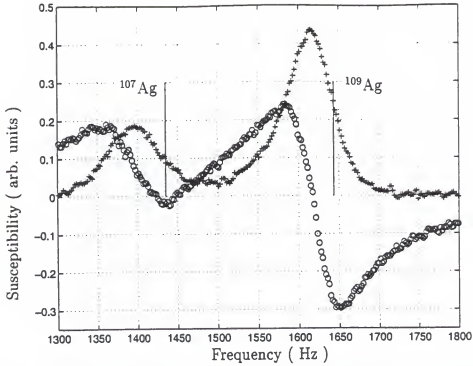


Figure 3.1: A frequency sweep at $B = 825.4 \mu\text{T}$ showing the downshift and suppression/enhancement of the silver signal as described in the text. The solid lines mark the unshifted resonance frequencies.

The solutions for the steady-state magnetizations with no relaxation take the form

$$m^{107}/B_1 = \gamma_{107} M_0^{107} \frac{\omega'_{109} - \omega + \gamma_{109}(R - 1/6)\mu_0 M_0^{109}}{(\omega - \omega_+)(\omega - \omega_-)} \quad (3.10)$$

and

$$m^{109}/B_1 = \gamma_{109} M_0^{109} \frac{\omega'_{107} - \omega + \gamma_{107}(R - 1/6)\mu_0 M_0^{107}}{(\omega - \omega_+)(\omega - \omega_-)}. \quad (3.11)$$

The intensities of the two modes shown in Figure 3.1 are not equal, nor do they scale as the ratio of the nuclear moments of the ^{107}Ag and ^{109}Ag spins. This result can be understood by studying the response functions found above at resonance.

At the lower mode ω_- , for the ^{107}Ag spins one has

$$m^{107}/B_1 = -\gamma_{107} M_0^{107} \frac{\omega'_{109} - \omega_- + \gamma_{109}(R - 1/6)\mu_0 M_0^{109}}{(\omega_+ - \omega_-)} \delta(\omega - \omega_-), \quad (3.12)$$

where $\delta(x)$ is the delta function.

The numerator can be expanded as

$$= 1/2 \left[\omega'_{109} - \omega'_{107} + \sqrt{(\omega'_{109} - \omega'_{107})^2 + 4\gamma_{107}\gamma_{109}(R - 1/6)^2\mu_0^2 M_0^{107} M_0^{109}} \right] \quad (3.13)$$

$$+ \gamma_{109}(R - 1/6)\mu_0 M^{109},$$

$$\approx \omega'_{109} - \omega'_{107} + \frac{\gamma_{107}\gamma_{109}(R - 1/6)^2\mu_0^2 M_0^{107} M_0^{109}}{\omega'_{109} - \omega'_{107}} \quad (3.14)$$

$$+ \gamma_{109}(R - 1/6)\mu_0 M^{109}, \quad (3.15)$$

$$> 0.$$

This last expression is greater than zero, so that the overall response of the ^{107}Ag nuclear spins at ω_- is negative. Performing a similar calculation for the ^{109}Ag spins, one finds that their response is positive. Extending this to the ω_+ mode, the ^{107}Ag and ^{109}Ag responses are found to be negative. The result is outlined in Figure 3.2. The important point is that the higher frequency mode is now identified with an *in-phase* precession of both the ^{107}Ag and ^{109}Ag nuclear spins, while the lower frequency mode is shown to be where the ^{109}Ag nuclear spins precess *out of phase* with respect to the ^{107}Ag spins. The sum of the two responses reproduces the features of Figure 3.1, where there is an overall enhancement of the signal intensity of the upper mode, and a suppression of the intensity of the lower mode.

3.1.2 Foil Geometry

The experiment in this work has a sample with a foil geometry and uses a linear excitation. The demagnetization factor has only one non-zero component, $D_{xx} = -1$, which breaks rotational symmetry. The linear excitation field is now given by $\vec{B}_{exc} = B_1(0, 0, \sin(\omega t))$.

In the case of the wire geometry, the resulting magnetizations are circularly polarized. This arises due to the neglect of the counter-rotating component of the excitation field in converting the linear excitation to a rotating one. The complete

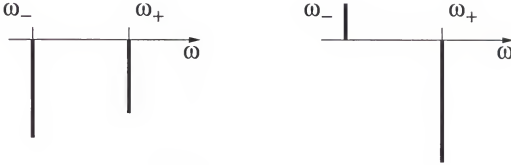
m_{107}/B_1 m_{109}/B_1 

Figure 3.2: Relative signs of the ^{107}Ag and ^{109}Ag nuclear spins at the resonance frequencies.

solution would have an elliptically precessing magnetization even for the rotating excitation. The inclusion of relaxation terms further complicates matters, as two different phase shifts are then required to completely describe the magnetizations in the \hat{x} and \hat{z} directions. With these considerations in mind, the steady-solutions for the foil geometry take the form

$$M_x^{107} = m_{107} \cos(\omega t + \alpha), \quad (3.16)$$

$$M_z^{107} = r_{107} m_{107} \sin(\omega t + \beta), \quad (3.17)$$

$$M_x^{109} = m_{109} \cos(\omega t + \gamma), \quad (3.18)$$

$$M_z^{109} = r_{109} m_{109} \sin(\omega t + \delta), \quad (3.19)$$

where the r 's and phase shifts α , β , γ , and δ describe the elliptical response of the magnetizations. Substituting these solutions into the Bloch equations for the foil

geometry, one obtains the substantial system of equations

$$\begin{bmatrix}
 \omega & 1/\tau_{107} & -A_x & 0 & 0 & 0 & B_x & 0 \\
 -1/\tau_{107} & \omega & 0 & -A_x & 0 & 0 & 0 & B_x \\
 -A_z & 0 & \omega & 1/\tau_{107} & B_z & 0 & 0 & 0 \\
 0 & -A_z & -1/\tau_{107} & \omega & 0 & B_z & 0 & 0 \\
 0 & 0 & C_x & 0 & \omega & 1/\tau_{109} & -D_x & 0 \\
 0 & 0 & 0 & C_x & -1/\tau_{109} & \omega & 0 & -D_x \\
 C_z & 0 & 0 & 0 & -D_z & 0 & \omega & 1/\tau_{109} \\
 0 & C_z & 0 & 0 & 0 & -D_z & -1/\tau_{109} & \omega
 \end{bmatrix}
 \begin{bmatrix}
 m_{107} \cos(\alpha) \\
 m_{107} \sin(\alpha) \\
 r_{107} m_{107} \cos(\beta) \\
 r_{107} m_{107} \sin(\beta) \\
 m_{109} \cos(\gamma) \\
 m_{109} \sin(\gamma) \\
 r_{109} m_{109} \cos(\delta) \\
 r_{109} m_{109} \sin(\delta)
 \end{bmatrix}$$

$$= B_1 \begin{bmatrix}
 \gamma_{107} M_0^{107} \\
 0 \\
 0 \\
 0 \\
 \gamma_{109} M_0^{109} \\
 0 \\
 0 \\
 0
 \end{bmatrix}. \quad (3.20)$$

The various terms are

$$\begin{aligned}
 A_x &= \gamma_{107} (B_0 + (R + 1/3) \mu_0 M_0^{109}), \\
 A_z &= \gamma_{107} (B_0 + (R + 1/3) \mu_0 M_0^{109} + \mu_0 M_0^{107}), \\
 B_x &= \gamma_{107} (R + 1/3) \mu_0 M_0^{107}, \\
 B_z &= \gamma_{107} (R - 2/3) \mu_0 M_0^{107}, \\
 C_x &= \gamma_{109} (R + 1/3) \mu_0 M_0^{109}, \\
 C_z &= \gamma_{109} (R - 2/3) \mu_0 M_0^{109}, \\
 D_x &= \gamma_{109} (B_0 + (R + 1/3) \mu_0 M_0^{107}), \quad \text{and} \\
 D_z &= \gamma_{109} (B_0 + (R + 1/3) \mu_0 M_0^{107} + \mu_0 M_0^{109}).
 \end{aligned}$$

As the pick-up coil in this experiment is parallel to the \hat{x} -axis, the detected signal is given by

$$M_{107}^x + M_{109}^x = m_{107} \cos(\omega t + \alpha) + m_{109} \cos(\omega t + \gamma)$$

$$\begin{aligned}
&= -[m_{107} \sin(\alpha) + m_{109} \sin(\gamma)] \sin(\omega t) \\
&\quad + [m_{107} \cos(\alpha) + m_{109} \cos(\gamma)] \cos(\omega t).
\end{aligned} \tag{3.21}$$

While it is not practical to write out the full closed form solution to the above system of equations, for the case of no relaxation ($\tau \rightarrow \infty$), a similar analysis as for the wire geometry can be carried out. The ratio of the signal intensities for the ^{109}Ag and ^{107}Ag modes is found to be

$$r = -\frac{\gamma_{107} M_0^{107} \Omega_{1+} + \gamma_{109} M_0^{109} \Omega_{2+}}{\gamma_{107} M_0^{107} \Omega_{1-} + \gamma_{109} M_0^{109} \Omega_{2-}} \tag{3.22}$$

where

$$\begin{aligned}
\Omega_{1+} &= \omega_+^2 - D_x D_z - A_z C_x - D_x C_z - B_z C_x, \\
\Omega_{2+} &= \omega_+^2 - A_x A_z - A_x B_z - D_z B_x - B_x C_z, \\
\Omega_{1-} &= \omega_-^2 - D_x D_z - A_z C_x - D_x C_z - B_z C_x, \\
\Omega_{2-} &= \omega_-^2 - A_x A_z - A_x B_z - D_z B_x - B_x C_z,
\end{aligned}$$

and the eigenfrequencies for the foil geometry take the form

$$\begin{aligned}
\omega_{\pm}^2 &= \frac{1}{2} [(A_x A_z + D_x D_z) + 2B_x C_z \pm ((A_x A_z - D_x D_z)^2 + 4[(A_x A_z + D_x D_z) B_x C_z \\
&\quad + A_x D_x B_z C_z + A_z D_z B_x C_x])^{1/2}].
\end{aligned} \tag{3.23}$$

The ratio of the line intensities is a function of the static field B_0 and the p . Given B_0 and the ratio, the polarization can be determined.

3.2 Spin-flip Equations of Motion

In conventional pulsed NMR, the magnetization can be inverted with a 180° pulse with an excitation frequency ω_{exc} equal to the Larmor frequency ω_0 . However, for

extremely short pulses (one or two periods long) where the excitation field B_{exc} is on the order of the static field B_0 , this is no longer the case. The experiment by Friedmann and co-workers [20] illustrates that for single-period pulses, the tipping frequency should be greater than the Larmor frequency. For square-wave pulses, this is $\omega_{exc} = \sqrt{2}\omega_0$, as they have shown.

In silver, the situation is complicated owing to the presence and interaction of the two isotopes ^{107}Ag and ^{109}Ag . At low fields, where the two resonance lines have exchange merged [3] into one, even a single period pulse turns out to be too long in comparison to T_2 to efficiently flip the magnetization. The calculation described in this section maps out the inversion efficiency as a function of tipping field and frequency in silver. The optimal efficiency is found to occur for tipping frequencies greater than the average Larmor frequency of the two lines, in qualitative agreement with the results of Friedmann. However, it is very close to the frequency of the ^{109}Ag mode, due to the coupling between the two isotopes.

The full equations of motion for a finite tipping pulse are described by the Bloch equations. A suitable change of coordinate system allows the inclusion of relaxation terms in the description. These are important as $T_2 \sim 10$ ms in silver, and the experimental frequency range of this work is only 1 to 1.5 kHz, at which even a single-period tipping pulse lasts for ~ 1 ms.

The starting point for the description of the tipping spin dynamics is the Bloch equations. However, unlike the usual case of pulsed NMR, where a transformation [6] is made to the rotating frame, we keep the full set of equations and solve them numerically. The usual trick describes the tipping field as a rotating magnetic field when it is actually a linear field. This transformation ignores the counter-rotating component of the tipping field, which is important in this case [38].

3.2.1 Relaxation Terms

The magnetization relaxes due to spin-lattice (T_1) and spin-spin (T_2) interactions. For the experiments in this work, T_1 is effectively infinite due to the very low experimental temperatures, and can be ignored. T_2 , on the other hand, is approximately 10 ms. As the experimental frequencies are on the order of $f \sim 1$ kHz, and $1/T_2 \sim 16$ Hz, the relaxation of the magnetization from T_2 processes has to be included in the equations of motion to correctly describe the spins during a tipping pulse. It is easiest to consider only one spin species to determine how the spin-spin relaxation enters in the finite tipping pulse case. Then, the method outlined will be applied to the case in silver, yielding the full coupled equations of motion.

The total applied magnetic field is the sum of the DC and excitation fields

$$\vec{B}_{total} = \vec{B}_0 + \vec{B}_{exc}, \quad (3.24)$$

where $\vec{B}_0 = (0, 0, B_0)$ and $\vec{B}_{exc} = (B_1 \sin(\omega t), 0, 0)$. In the standard transformation [13, 17] from the lab frame to the rotating frame, \vec{B}_0 is replaced by

$$\vec{B}_0 + \omega/\gamma \hat{z}. \quad (3.25)$$

For most NMR work, the excitation field is considered to be a superposition of two counter-rotating fields of magnitude $B_1/2$ with frequencies $\pm\omega$. At resonance, when $\omega \sim \gamma B_0$, the component at frequency $-\omega$ will be off resonance by 2ω , and can be ignored. However, when $B_1 \sim B_0$, this approximation breaks down. To account for this, a transformation of the Bloch equation must be made to the ‘rocking’ frame (shown in Figure 3.3). This introduces another effective field term . It also allows the incorporation of the T_2 relaxation in a straightforward manner. The equations in the rocking (primed) frame now take the form

$$\dot{M}_{z'} = M_{x'}\dot{\theta} \quad (3.26)$$

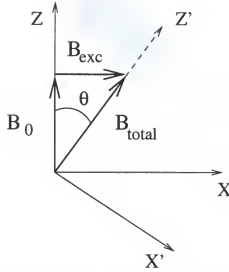


Figure 3.3: Relation between the effective and static field. The Y and Y'-axes are the same, and point into the page.

$$\dot{M}_{x'} = -M_{x'}\dot{\theta} + \gamma M_{y'} B_{total} - \frac{M_{x'}}{T_2} \quad (3.27)$$

$$\dot{M}_{y'} = -\gamma M_{x'} B_{total} - \frac{M_{y'}}{T_2}. \quad (3.28)$$

From the field geometry in Figure 3.3, one has that

$$\tan \theta = \frac{B_1 \sin(\omega t)}{B_0}. \quad (3.29)$$

Taking the time derivative of both sides yields

$$\dot{\theta} = \frac{B_1/B_0 \omega \cos(\omega t)}{1 + (B_1/B_0)^2 \sin^2(\omega t)}. \quad (3.30)$$

The total field B_{total} is now given by

$$B_{total} = \sqrt{B_0^2 + B_1^2 \sin^2(\omega t)}. \quad (3.31)$$

The transformation back to the lab frame is effected by

$$M_z = M_{x'} \cos \theta - M_{y'} \sin \theta, \quad (3.32)$$

$$M_x = M_{x'} \sin \theta + M_{y'} \cos \theta, \quad (3.33)$$

$$M_y = M_{y'}, \quad (3.34)$$

where the initial conditions are

$$M_{z'} = 1, \quad (3.35)$$

$$M_{x'} = 0, \quad (3.36)$$

$$M_{y'} = 0. \quad (3.37)$$

The coupled equations of motion for the silver nuclei can now be derived, using the previous equations as a guide. After some algebra, one finds that

$$\begin{aligned} \dot{M}_z^{109} = & (\cos \theta \sin \theta / T_2 + \gamma_{109} \mu_0 (R + 1/3) M_y^{107}) M_x^{109} \\ & - \gamma_{109} (B_1 \sin(\omega t) + \mu_0 (R + 1/3) M_x^{107}) M_y^{109} \\ & - \sin^2 \theta / T_2 M_z^{109}. \end{aligned} \quad (3.38)$$

$$\begin{aligned} \dot{M}_x^{109} = & -\cos^2 \theta / T_2 M_x^{109} + \gamma_{109} (B_0 + \mu_0 (R + 1/3) M_z^{107}) M_y^{109} \\ & + (\cos \theta \sin \theta / T_2 - \gamma_{109} \mu_0 (R + 1/3) M_y^{107}) M_z^{109}, \end{aligned} \quad (3.39)$$

$$\begin{aligned} \dot{M}_y^{109} = & -\gamma_{109} (B_0 + \mu_0 (R + 1/3) M_z^{107}) M_x^{109} - M_y^{109} / T_2 \\ & + \gamma_{109} (B_1 \sin(\omega t) + \mu_0 (R + 1/3) M_x^{107}) M_z^{109}, \end{aligned} \quad (3.40)$$

As the original set of equations is symmetric with respect to the two nuclear spin species, the results for ^{107}Ag can be obtained by making the substitution $^{107}\text{Ag} \leftrightarrow ^{109}\text{Ag}$.

These equations do not allow a closed form solution, and can only be numerically integrated. A program using The Student Edition of MATLAB IV¹ is used to perform the integration for different values of the parameters. In the simulation, the \hat{z} -component of the ^{107}Ag and ^{109}Ag magnetizations are used to characterize the efficiency of the tipping pulse. The total $M_z^{total} = M_z^{107} + M_z^{109}$ is compared before and after the pulse, giving a calculated efficiency of

$$e_{calc} = \frac{M_z^{total} \text{ after tipping pulse}}{M_z^{total} \text{ before tipping pulse}}. \quad (3.41)$$

¹MathWorks, Inc., 24 Prime Park Way, Natick, MA 01760-1500, Phone: (508) 647-7000

The results of the simulation show several key points. At low fields, where the Larmor frequency is ~ 100 Hz, the tipping efficiency for one and two period pulses is no better than 50%. This limitation occurs owing to the tipping frequency being comparable to T_2 , the spin-spin relaxation time. The pulse duration is long enough to allow considerable de-phasing to occur among the spins. The only way to increase the efficiency according to the simulation is to move to higher fields (and correspondingly higher tipping frequencies). At Larmor frequencies of ~ 1.5 kHz, the tipping efficiency from the simulation is found to be much higher, on the order of 80%. However, the optimum tipping frequency is not simply related to the resonance frequencies of the ^{107}Ag and ^{109}Ag spins for polarizations of at least 10%. To achieve a high efficiency inversion of the magnetizations of both silver isotopes, the tipping frequency must almost be as large as the resonance frequency of the ^{109}Ag mode.

3.3 Data Reduction

The output from the lock-in has been de-convoluted according to the following scheme:

1. The lock-in offset is subtracted from the raw data, background data, and calibration data.
2. A gain correction factor of 2.887 is made to the cosine channel of the lock-in output, to compensate for extra amplification in the sine channel.
3. The phase ϕ and amplitude A of the raw data, background data, and compensation data are calculated from $\phi = \arctan(y/x)$ and $A = \sqrt{x^2 + y^2}$ at each frequency, where x and y are the cosine and sine channels of the lock-in.

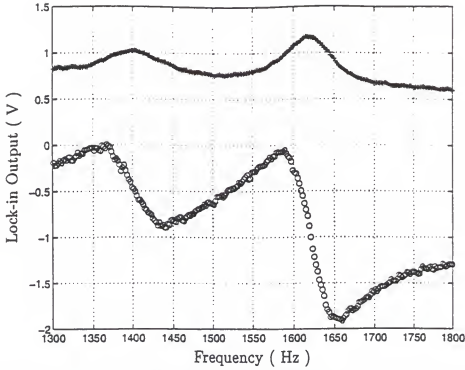


Figure 3.4: The lock-in output before data reduction. The cosine and sine channels of the lock-in are denoted by + and \bigcirc , respectively.

4. The phase and amplitude of the raw and background data are unmixed with the calibration data. This involves calculating new phase angles

$$\phi'_{\text{raw}} = \phi_{\text{raw}} - \phi_{\text{cal}} - \phi_{\text{offset}},$$

$$\phi'_{\text{background}} = \phi_{\text{background}} - \phi_{\text{cal}} - \phi_{\text{offset}},$$

where ϕ_{offset} is a phase correction of 0.51 radians. Both phases of the raw data are now reconstructed from

$$x = (A_{\text{raw}}/A_{\text{cal}}) \times \cos \phi'_{\text{raw}} \quad (3.42)$$

and

$$y = (A_{\text{raw}}/A_{\text{cal}}) \times \sin \phi'_{\text{raw}}. \quad (3.43)$$

The background signal is reconstructed in the same manner.

5. The background is then subtracted from the raw data.

A set of raw data is shown in Figure 3.4. The result of following the above steps is shown in Figure 3.5.

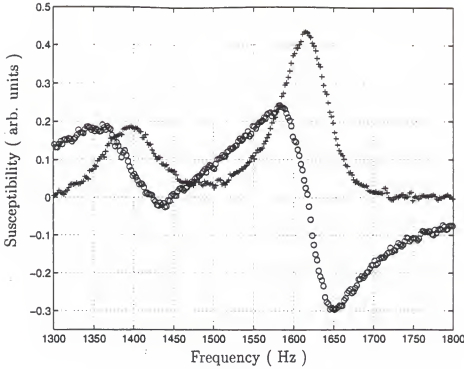


Figure 3.5: Processed data, as described in the text.

3.3.1 Field Calibration

The static field coil in the \hat{y} is calibrated by scaling the ^{107}Ag and ^{109}Ag peak frequencies at low polarization (~ 0.05) against their published gyromagnetic ratios. From [7], one finds

$$\begin{aligned} \frac{\gamma_{107}}{\gamma_{109}} &= \frac{1.732}{1.991} \\ &= 0.8699, \end{aligned} \tag{3.44}$$

where the ratio of the Knight-shifted values has been used. The peak frequencies are determined by fitting a double Lorentzian to both phases of the signal. The spectrum used for the field calibration is shown in Figure 3.6. The solid line is the result of a non-linear least squares fit to both phases using the Nelder-Mead simplex algorithm [39]. The ratio of the fitted resonance frequencies is

$$\frac{f_0^{107}}{f_0^{109}} = \frac{1443}{1659}$$

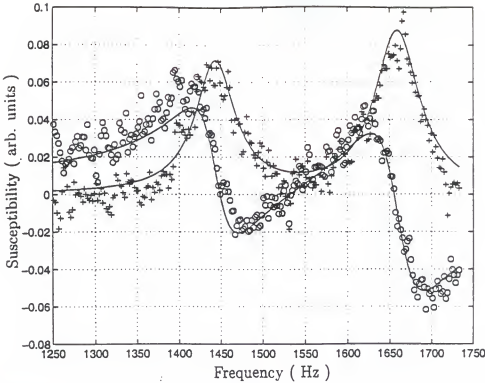


Figure 3.6: Data used to determine the horizontal static field calibration. Solid lines are the result of the fit described in the text.

$$= 0.8698 \quad (3.45)$$

which compares well with the accepted value. This gives a field-to-current ratio of $B/I = 3.55 \text{ mT/A}$. The calculated value from Table 2.2 is 3.55 mT/A .

The spin-spin relaxation times from the Lorentzian fit are 5.5 ms and 4.9 ms for ^{107}Ag and ^{109}Ag , respectively. These are smaller than the published [40] values of 9.1 ms and 10.4 ms . The discrepancy is accounted for by a field inhomogeneity of $\sim 1\%$, determined from

$$\frac{1}{T_2^*} = \frac{1}{T_2} + \gamma \Delta B, \quad (3.46)$$

where T_2^* is the experimentally determined spin-spin relaxation time, T_2 is the true spin-spin relaxation time, and ΔB is the spread in the static field.

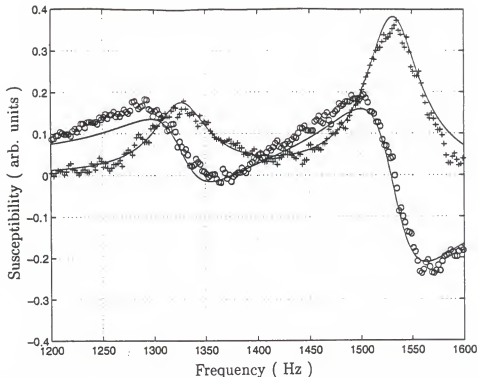


Figure 3.7: Spectrum used to set the polarization calibration. The solid line is the fit described in the text.

3.3.2 Polarization Calibration

The processed spectra are all fit to double Lorentzians as described in the previous section. The fitted lineshapes for the ^{107}Ag and ^{109}Ag modes are then integrated, and the intensity ratio of the two modes is used to determine the polarization as described at the end of section 3.1.2.

An attempt was made to measure the equilibrium polarization at $100\text{ }\mu\text{K}$. This would have provided an 'absolute' measure of the polarization to the integrated signal intensity. Unfortunately, the noise level is presently too large to determine this number. The polarization scale in this work has been set by selecting one spectrum and performing the above analysis to fix the polarization. The spectrum used to fix the polarization scale is shown in Figure 3.7. The solid lines are the fit to the data, which have been integrated to give the ratio of the line intensities. The measured lineshape falls off faster than the fit, indicating that the functional form is closer

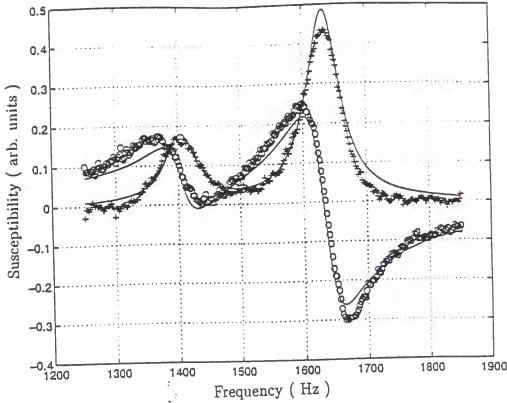


Figure 3.8: Initial magnetizations at positive temperature for the tipping sequence. Solid line is a Lorentzian fit to the data, which gives $p = 0.27$.

to a Gaussian, rather than Lorentzian, lineshape. The integration was carried out numerically using the trapezoid technique [41]. The static field for this data set is $777.4 \mu\text{T}$, and the signal intensity analysis yields a polarization $p = 0.27$. This gives a calibration constant of

$$\frac{p}{\text{area}} = 10.2 \times 10^{-3}. \quad (3.47)$$

3.4 Spin-flip Results

In Figure 3.8, a spectrum taken at $B_0 = 832.5 \mu\text{T}$ is shown. Figure 3.9 shows the magnetization after the application of a tipping pulse of frequency 1625 Hz applied for two periods with a vertical excitation field of $B_{\text{exc}} = 540 \mu\text{T}$ (from the calculated coil constant in Table 2.2). The initial polarization is $p_i = 0.27$, and is taken to be the same for both spin species. After tipping, the polarization from the integrated area is found to be $p_f = -0.22$, giving an efficiency of $\sim 81\%$. The magnitude of the

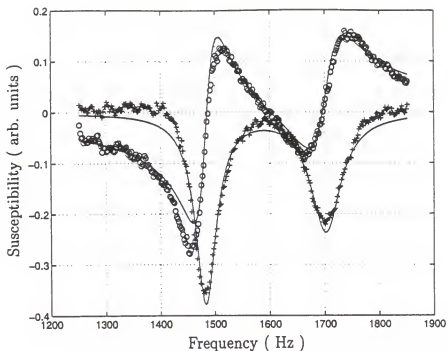


Figure 3.9: Spectrum after the tipping pulse described in the text. Solid line is a Lorentzian fit to the data, which gives $p = -0.22$.

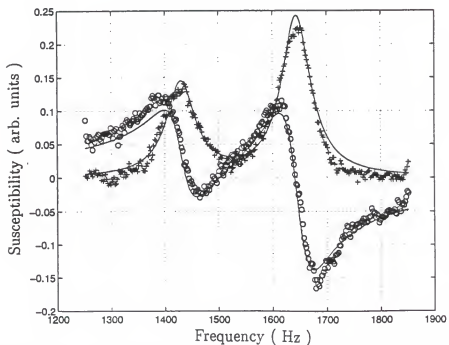


Figure 3.10: Final magnetizations at positive temperature for the tipping sequence. Solid line is a Lorentzian fit to the data, which gives $p = 0.16$.

tipping field is used as a fitting parameter to match the initial and final polarizations in the simulation, as there is no calibration of the excitation coil. Using a tipping field of $B_{exc} = 450 \mu\text{T}$ in the simulation, the final calculated polarization for the ^{107}Ag and ^{109}Ag spins is found to be $p_{calc} = -0.21$, yielding a model efficiency of 78%.

The magnetization is now flipped from negative temperature back to positive temperature by applying the same pulse as before. The resulting spectrum is shown in Figure 3.10. The final calculated polarization for the ^{107}Ag and ^{109}Ag spins is found to be slightly different, giving $p_{107} = 0.16$ and $p_{109} = 0.14$. The polarization determined from the integrated intensity is found to be $p = 0.16$.

CHAPTER 4 FUTURE WORK AND CONCLUSIONS

4.1 Higher Initial Polarization

The initial polarizations for the nuclear magnetization reported in this work are only of moderate value, being in the area of ~ 0.2 - 0.3 . From the discussion in Chapter 1, this is too low a starting point to reach the ordered state of the nuclear spins at negative temperatures, for which the zero-field critical polarization [15] is reported as $p_{crit} = 0.49$.

There are several modifications that can be tried to determine the cause of these low initial polarizations. In the current detection scheme, the final Larmor field applied to the sample is horizontal, while the field from the large second demagnetization magnet is vertical. This leads to the possibility of polarization loss due to inadequate control in the changing of the magnetic field orientation from vertical to horizontal at the end of the demag. To try and go smoothly from one orientation to the other, the small Larmor field coil in the vertical direction should be energized along with the horizontal field coil, towards the end of the second stage demag. The second stage magnet should then be ramped down in the normal way, after which the small vertical field can be reduced smoothly.

Another possibility is to swap the vertical excitation and horizontal static field coils. That is, use the horizontal static coil for the excitation field, and the vertical excitation coil for the static field, while keeping the same pick-up coil orientation. This is something that could be done rather easily from the top of the cryostat at room temperature. The only difficulties might arise from the large diameter-to-length ratio

of the vertical coil (about 5 to 1), giving poor field homogeneity and the possibility of a large phase shift in the excitation from the horizontal static coil. One ancillary benefit from the swapping of coils is that it could enable the calibration of the current-to-field ratio of the excitation coil. This would remove one fitting parameter from the tipping simulation.

4.2 Conclusions

In this work, a new technique has been developed to generate high efficiency inversions of the nuclear magnetization in metals. The experimental results in silver have been found to be in good agreement with the model developed from the Bloch equations using a linear excitation field and incorporating the RK exchange interaction between the nuclear moments. The best experimental inversion efficiency achieved in this work is $\sim 81\%$ for a starting polarization $p = 0.27$, yielding a final polarization of $p = -0.22$. This technique has not yet been fully optimized, as the simulation shows that the inversion efficiency increases at higher static fields for a suitable choice of tipping frequency and magnitude. With this new scheme, it should be possible to reach the ordered state of the silver nuclear moments at negative temperatures, and determine the phase diagram.

APPENDIX A SUSCEPTIBILITY MEASUREMENT OF PrBe_{13}

This appendix is a brief summary of work done on the hyperfine-enhanced nuclear paramagnet PrBe_{13} . The first part of this section describes the experimental apparatus used in the susceptibility measurements, along with the results. The next part gives a brief introduction to the physics of this material, and presents the results of a mean field calculation used to interpret the data.

A.1 Introduction

Hyperfine enhanced Van Vleck paramagnets have been a subject of interest to the low temperature community for a number of years. Their use as possible nuclear refrigerants [42] for low temperature cryostats, along with the interesting physics [43] in these systems, has made them an ongoing field of study.

Recent work by Hiess and co-workers [47] on the NpBe_{13} system has highlighted the possibility of understanding the heavy-fermion (HF) superconductor UBe_{13} by studying the other rare-earth and actinide Metal- Be_{13} compounds. These systems have a cubic NaZn_{13} structure, where the Metal component occupies the sites of a simple cubic lattice. All of the Uranium based HF compounds are found to order antiferromagnetically, with $T_N > T_c$, with the glaring exception being UBe_{13} [48, 49]. That is, except for UBe_{13} , the other Uranium based HF's all exhibit strong magnetic correlations. The neutron scattering work of Hiess and co-workers finds a magnetic wave vector $\vec{q} = (1/3 \ 0 \ 0)$ for NpBe_{13} , the same as found in several other of the

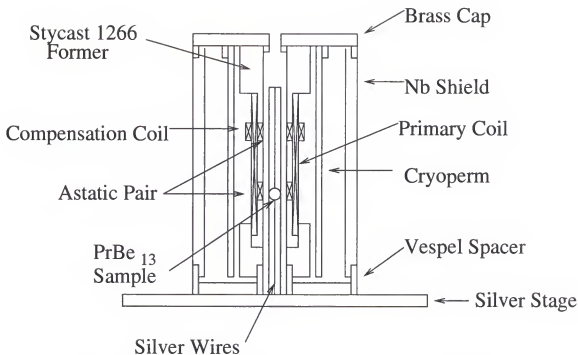


Figure A.1: Silver platform and coils for the PrBe_{13} experiment.

Metal- Be_{13} systems [47]. They suggest that this is the wave vector that should be searched for magnetic correlations in UBe_{13} .

This leads to the interesting possibility of understanding the magnetism in UBe_{13} through studying the magnetic structure of PrBe_{13} . Of all the Metal- Be_{13} compounds, PrBe_{13} is unique, as it is the $4f$ analog of UBe_{13} . The electronic configuration of U^{4+} is $5f^2$ (assuming it is not in a mixed-valence state), while Pr^{3+} has a configuration of $4f^2$. Neutron scattering experiments on PrBe_{13} should provide interesting information relevant to the physics of UBe_{13} .

Previous work on PrBe_{13} has been focused on high temperatures [44, 45], where only the ionic moments of the system have been studied, or to methods [46] where the interaction between the Pr nuclear moments was indirectly determined. The experiment described here directly probes the Pr nuclear spin interaction.

A.1.1 Sample and Experimental Apparatus

The zero-field nuclear magnetic susceptibility of PrBe_{13} was measured with a mutual inductance technique [50] using a DC SQUID sensor. The polycrystalline sample weighs 3.17 mg, and has a volume of $\sim 1 \text{ mm}^3$. The sample was provided by Professor G. R. Stewart of the University of Florida.

A stand (see Figure A.1) consisting of four bunched silver wires welded to a silver plate formed the thermal link and sample holder for the PrBe_{13} . The sample was glued to the wires using Epo-Tek¹ conductive silver paint. The stand was bolted to the top of the copper nuclear demagnetization cryostat, with the wires and sample inserted into the excitation and detection coils.

The experimental coil arrangement is outlined in Figure A.1. The sample is centered in the top of an astatic pair of pick-up coils. As the wire forms a closed superconducting loop, flux is conserved on the detection side of the circuit. The total flux in this part can be written as

$$\phi = (M_{p_1}(1 + \chi) + M_{p_2})i_p + M_{c_2}i_c, \quad (\text{A.1})$$

where M_{p_1} is the mutual inductance between the primary coil and the first astatic coil, M_{p_2} is the mutual inductance between the primary coil and second astatic coil, M_{c_2} is the mutual inductance between the compensation coil and second astatic coil, and i_p and i_c are the currents in the primary and secondary coils. The mutual inductance between the primary and first astatic pair is modified by the presence of the magnetic sample by a factor of $(1 + \chi(T))$, where $\chi(T)$ is the temperature dependent susceptibility of the nuclear moments. Denoting the inductances in the detection part of the circuit as L_1, L_2 and L_3 , the total flux can also be written as

$$\phi = (L_1 + L_2 + L_3)i_s, \quad (\text{A.2})$$

¹Epoxy Technology Inc., 14 Fortune Dr., Billerica, MA 01821.

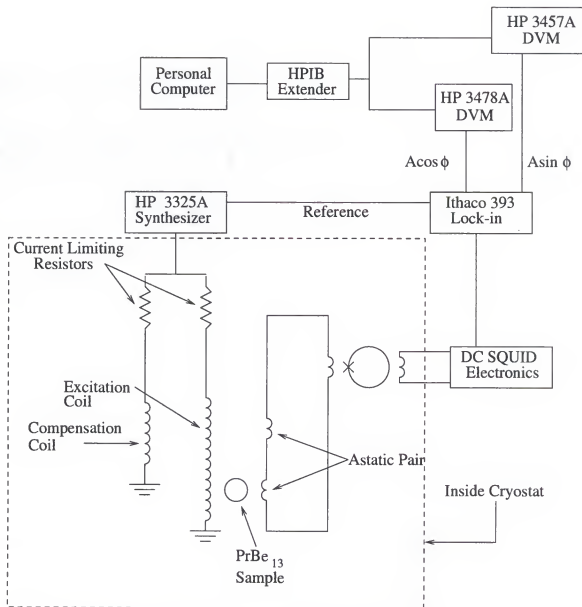


Figure A.2: Schematic of the electronics for the PrBe₁₃ experiment.

where i_s is the super-current flowing in the circuit. These equations can be combined to find

$$\delta\chi = \frac{\delta i_s \sum L_i}{i_p M_{p1}}. \quad (\text{A.3})$$

δi_s is related to the DC SQUID output voltage, which the manufacturer gives as 1.832×10^{-5} A/V. The mutual inductance M_{p1} is $3.3 \mu\text{H}$, and the total inductance $\sum L_i$ is $4.9 \mu\text{H}$. The primary current is just $i_p = V_{exc}/R_p$, where V_{exc} is the excitation voltage from the HP synthesizer, and R_p is the current limiting resistor to the excitation coil. The excitation voltage was set at $0.6 V_{pp}$. The excitation field used in this work has an amplitude of $2.64 \mu\text{T}_{pp}$ at a frequency of 9.23 Hz . With this in hand, one can convert the lock-in voltage to a susceptibility.

Figure A.3 shows the results of the measurement. The susceptibility has a cusp at $T_N = 0.40 \text{ mK}$, indicating that the Pr nuclear moments have ordered antiferromagnetically. The high temperature part of the nuclear susceptibility data was fitted to a Curie-Weiss form, plus a constant background term. A non-linear least squares fit to the data at high temperature yields a Weiss temperature $\Theta = -2.2 \text{ mK}$. The results of the fit are shown in Figure A.3. This measured Weiss temperature is in contradiction to the ESR g-shift result [46], which found a weak ferromagnetic interaction corresponding to $\Theta = 60 \mu\text{K}$.

A.2 Mean Field Calculation for T_N

In the mean field theory, the ratio of the Weiss to the Neel temperature, Θ/T_N , can be used to determine the arrangement of the moments in the ordered state. The structure that our experimental result implies has been calculated using a mean field theory incorporating nearest-neighbor (nn) and next-nearest-neighbor (nnn) interactions on a simple cubic lattice. The procedure used follows that outlined by Smart [51], and is in agreement with the result of ter Haar [52].

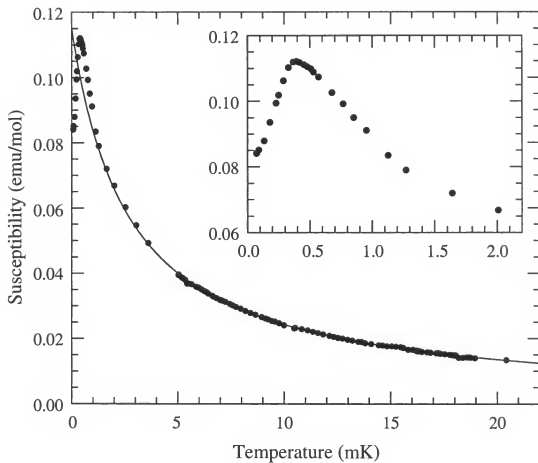


Figure A.3: Nuclear susceptibility of PrBe_{13} . Solid line is the non-linear least squares fit to the high temperature data from 5 to 20 mK. The ordering transition is shown in the inset.

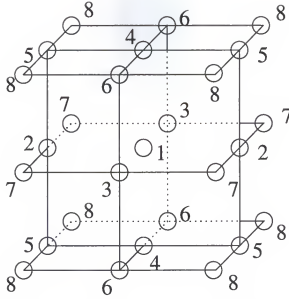


Figure A.4: Division of the cubic lattice into eight sub-lattices, as described in the text.

The Heisenberg Hamiltonian for the nuclear spins is of the form

$$H = - \sum_{i < j} J_{ij} \vec{I}_i \cdot \vec{I}_j, \quad (\text{A.4})$$

where J_{ij} is the exchange interaction between spins i, j , and the \vec{S} are spin angular momentum operators. The lattice is divided up into $n = 8$ sub-lattices relative to the center spin 1, such that no interactions take place between any neighbors on their own sub-lattice. The division of spins is shown in Figure A.4, where the numbers denote the sites belonging to each sub-lattice. Note that the sub-lattice corresponding to number 8 is for next-next-nearest-neighbors, for which the interactions are zero. It is introduced only for convenience [51] in the following calculations.

The total magnetic field acting on the i^{th} sub-lattice is given by

$$\vec{H}_i = \vec{H}_0 + \sum_{j=1}^n \gamma_{ij} \vec{M}_j, \quad (\text{A.5})$$

where \vec{H}_0 is the external field, \vec{M}_j is the magnetization of the j^{th} sub-lattice, and γ_{ij} is the coupling between the sub-lattices. All self-coupling terms of the form γ_{ii} are

taken to be zero. In terms of the Hamiltonian, one has

$$\gamma_{ij} = n(z_{ij}J_{ij}/(N_A(g_n\mu_n)^2), \quad (\text{A.6})$$

where z_{ij} is the number of j neighbors of spin i , μ_n is the nuclear magneton, N_A is Avogadro's number, g_n is the Lande g -factor, and n is the number of sub-lattices. The usual mean field coefficients are related to these γ 's by $\gamma_{ij} = f_{jk}^i \gamma_i$, where f_{jk}^i is the fraction of the i^{th} nn 's of spin j on sub-lattice k . The normal mean field coefficients are found to be

$$\gamma_{nn} = 3z_{nn}J_{nn}/(N_A(g_n\mu_n)^2), \quad (\text{A.7})$$

where z_{nn} is the number of nearest neighbors and J_{nn} is the interaction strength between nearest neighbors. The form of γ_{nnn} is obtained by replacing nn with nnn in the above equation.

By putting the external field \vec{H}_0 equal to zero in equation A.5, one obtains a set of equations relating the sub-lattice magnetizations and their local fields. The eigenvalues of this set of equations yield the possible mean field ordering temperatures for the magnetic moments.

The ordering temperatures as a function of the mean field coefficients are found to be

$$T_1 = (\gamma_{nnn} - \gamma_{nn})C, \quad (\text{A.8})$$

$$T_2 = -1/3(\gamma_{nn} + \gamma_{nnn})C, \quad (\text{A.9})$$

$$T_3 = 1/3(\gamma_{nn} - \gamma_{nnn})C, \quad \text{and} \quad (\text{A.10})$$

$$T_4 = (\gamma_{nn} + \gamma_{nnn})C, \quad (\text{A.11})$$

where $C = N_A\mu_0(g_n\mu_n)^2I(I+1)/(3k_B)$ is the nuclear Curie constant. The Weiss temperature is $\Theta = (\gamma_{nn} + \gamma_{nnn})C$, corresponding to the temperature T_4 . Ordering temperatures one, two, and three correspond to different possible antiferromagnetic structures. The structure corresponding to T_3 can be eliminated as it describes an

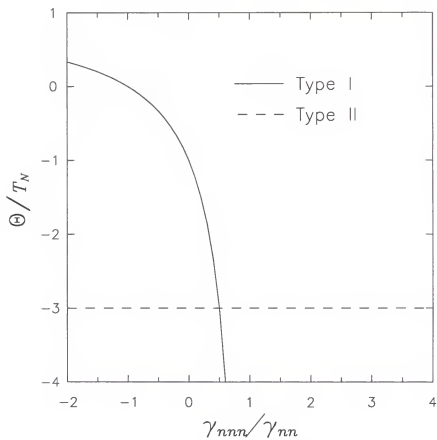


Figure A.5: The ratio of the Weiss and Neel temperatures as a function of the mean field coefficients and the spin configurations for.

energetically unfavorable arrangement of spins, as compared to the Neel temperatures T_1 and T_2 .

In Figure A.5, the ratio of the Weiss temperature Θ to the Neel temperature T_N is plotted as a function of the mean field coefficients γ , and the dashed and solid lines correspond to T_1 and T_2 , respectively. The lowest energy configurations for the spins correspond to the upper branches of the plot. The results of the calculation show that the ground state for the nuclear spins is of the Type II structure for $\gamma_{nnn}/\gamma_{nn} > 1/2$, while for $\gamma_{nnn}/\gamma_{nn} < 1/2$ the ordered structure is Type I. From the data, one finds that $\Theta/T_N \sim -6$, which implies antiferromagnetic interactions between nnn and a Type II ordered structure for the Pr^{3+} nuclear moments. The large value (by about a factor of 2) of the experimentally determined ratio as compared to the result of the calculation suggests that the transition is not mean field like, and fluctuations are important.

APPENDIX B

CW NMR MEASUREMENTS ON GOLD

Two different high purity gold samples were studied. For both samples, no NMR signal was detected. The following sections describe the experimental geometry of the gold samples, and the heat treatments used to prepare them. The electronics and NMR coils used for the gold experiments are the same as those described in chapter 2.

B.1 Gold Fan Stage

The thermal link between the bottom of the copper demagnetization stage and this sample consisted of a four 9's purity gold sheet¹ that was folded over seven times into the shape of a fan. The width of the folds was 0.25 inches, and the overall length of the fan was 6.86 inches. The five 9's purity gold sample² consisted of 16 foils $0.1 \text{ mm} \times 3 \text{ mm} \times 50 \text{ mm}$. These were cut from a $50 \text{ mm} \times 50 \text{ mm} \times 0.1 \text{ mm}$ sheet with a pair of ceramic scissors. The foils were diffusion welded into the bottom end of the fan, with the overlap of the sample and fan being 10 mm. The top part of the gold fan was diffusion welded to a set of nine silver fins ($1.125 \text{ in} \times 0.2 \text{ in} \times 0.016 \text{ in}$) that were TIG-welded into the silver base attached to the bottom of the copper demagnetization stage. The overlap between the silver fins and the gold fan was 1 in.

The gold fan, gold sample, and silver base were all annealed separately before diffusion welding. The silver stage was annealed for 10 hours at a temperature of 750°C

¹A.D. MACKAY, Inc., 10 North Broadway, P.O. Box G, Red Hook NY 12571.

²Aesar, 892 Lafayette Road, P.O. Box 1087, Seabrook, NH 03874-1990.

Table B.1: Annealing results for gold foils.

RUN	T (°C)	P _{O₂} (Torr)	time	RRR	Comments
1	900	—	26 hours	100	annealed in air
2	925	10 ⁻⁴	21 hours	140	—
3	965	10 ⁻⁴	7 days	365	—
4a	965	10 ⁻⁴	10.25 days	445	—
4b	965	10 ⁻⁴	16.6 days	488	—
4c	965	10 ⁻⁴	20.1 days	445	cumulative time on sample 4

under an oxygen pressure of 3×10^{-4} torr. The results of various heat treatments on gold foils are summarized in Table B.1. The gold sample foils were annealed for 9 days at 950 °C under an oxygen pressure of 10^{-4} torr. The gold fan was annealed in the same fashion, except that small quartz slides were placed in the folds of the fan to keep it from welding itself together during the heat treatment.

The sample foils were then diffusion welded to the end of the gold fan. A small stainless steel clamp with quartz slide 'jaws' was used to hold the sample foils and fan in place. This heat treatment was done at 900 °C for ten hours under vacuum ($\sim 4 \times 10^{-6}$ torr). At some point during the diffusion welding, a leak opened up in the system, resulting in an oxide layer (from the stainless steel clamp) forming on the gold sample. This was removed using a mild solution of HBr. The gold fan was then diffusion welded to the silver fins by cooking at 660 °C for 12 hours under an oxygen pressure of 10^{-4} torr. After cleaning, the gold foils were clean enough to stick to each other on contact. In order to keep the foils separate, a silicon oxide powder (six 9's pure) from Alpa-Aesar was sprinkled on the foils. The powder adhered lightly to the gold, but was sufficient to keep the foils from bonding to each other.

B.2 NIST gold sample

The second gold experiment used the same design of silver thermal link as in the silver experiment. The geometry of both experiments is identical, the only difference being that the silver sample foils in Figure 2.2 are replaced by gold foils.

A small, high purity (six 9's) gold rod was purchased from NIST³ (Standard Reference Material 685). At first, several attempts were made to roll the gold into a foil. These were unsuccessful, as the material work hardened to such an extent that it could not be flattened to any appreciable degree. It was found that the gold could be rendered malleable by heating at 150 °C in air for one hour. The sample was cut into several smaller pieces with a ceramic knife. These were rolled to ~ 0.1 mm thickness using the mechanical roller in the Materials Science machine shop. In order to prevent contamination from the steel rollers, the gold was sandwiched between two sheets of molybdenum⁴ of three 9's purity. The gold sheets obtained from this rolling were then cut into 16 foils 3 mm wide and 50 mm long with a pair of ceramic scissors.

The heat treatment of these foils was straightforward, as it was found that RRR's of over 1000 could be obtained by annealing in air for 2.5 hours at 700 °C. The sample was annealed for 3 days at 900 °C under an oxygen pressure of 10^{-4} torr. This procedure yielded a RRR of 1700. The foils were welded to the bottom of the silver cross with an acetylene torch. After welding, the foils were dusted with silicon oxide powder to prevent them from sticking together.

B.3 Experimental Search

The procedure outlined in chapter 2 for the silver experiment was used in the search for the gold NMR signal. The absence of a signal led to a very large search in frequency, however. A large number of sweeps were made at frequencies in the

³NIST, US Department of Commerce, Gaithersburg, MD 20899.

⁴Schwarzkopff Technologies Corp., 35 Jeffrey Ave., Holliston, MA 01746.

region of 1 kHz for various static fields. As no gold signal was observed in this region, several attempts were made to observe the NMR signal by demagnetizing the second magnet straight to zero-field, and searching for a resonance from 10 to 100 Hz. In this regime, no signal could be found. For the second gold experiment only, an attempt was made to measure the equilibrium magnetization at 3 kHz at a temperature of 100 μ K. Unfortunately, no NMR signal was detected in this scheme, either. For the time being, the observation of the CW NMR signal in gold remains an open topic.

REFERENCES

- [1] J. P. Ekstrom, J. F. Jacquinet, M. T. Loponen, J. K. Soini, and P. Kumar, *Physica* **98B**, 45 (1979).
- [2] M. T. Huiku, T. A. Jyrkkio, J. M. Kyynarainen, A. S. Oja, and O. V. Lounasmaa, *Phys. Rev. Lett.* **53**, 1692 (1984).
- [3] A. S. Oja, A. J. Annila, and Y. Takano, *Phys. Rev. B* **38**, 8602 (1988).
- [4] A. S. Oja, A. J. Annila, and Y. Takano, *J. Low Temp. Phys.* **85**, 1 (1991).
- [5] M. A. Ruderman and C. Kittel, *Phys. Rev.* **96**, 99 (1954).
- [6] A. Abragam, *The Principles of Nuclear Magnetism*, (Clarendon Press, Oxford, 1961).
- [7] G. C. Carter, L. H. Bennett, and D. J. Kahan, *Metallic Shifts in NMR*, (Pergamon Press, Oxford, 1977).
- [8] P. J. Hakonen, S. Yin, and K. K. Nummila, *Europhys. Lett.* **15**, 677 (1991).
- [9] K. K. Nummila, J. T. Tuoriniemi, R. T. Vuorinen, O. V. Lounasmaa, K. Lefmann, K. N. Clausen, A. Metz, K. Siemensmeyer, L. Lipinski, M. Steiner, and F. B. Rasmussen, *Czech. J. Phys.* **46**, 2201 (1996).
- [10] P. J. Hakonen, O. V. Lounasmaa, and A. Oja, *J. Magn. Magn. Mater.* **100**, 394 (1991).
- [11] M. T. Huiku, and M. T. Loponen, *Phys. Rev. Lett.* **49**, 1288 (1982).
- [12] P. J. Hakonen, S. Yin, and O. V. Lounasmaa, *Phys. Rev. Lett.* **64**, 2707 (1990).
- [13] A. Abragam and M. Goldman, *Nuclear Magnetism: Order and Disorder*, (Clarendon Press, Oxford, 1970).
- [14] P. Kumar, to be published.
- [15] P. J. Hakonen, K. K. Nummila, R. T. Vuorinen, and O. V. Lounasmaa, *Phys. Rev. Lett.* **68**, 365 (1992).
- [16] P. J. Hakonen, R. T. Vuorinen, and J. E. Martikainen, *Phys. Rev. Lett.* **70**, 2818 (1993).

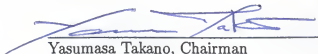
- [17] C. P. Slichter, *Principles of Magnetic Resonance*, (Springer-Verlag, Berlin, 1989).
- [18] E. M. Purcell and R. V. Pound, *Phys. Rev.* **81**, 279 (1951).
- [19] A. S. Oja, A. J. Annala, and Y. Takano, *J. Low Temp. Phys.* **85**, 1 (1991).
- [20] L. J. Friedmann, A. K. Wennberg, S. N. Ytterboe, and H. M. Bozler, *Rev. Sci. Instrum.* **57**, 410 (1986).
- [21] O. V. Lounasmaa, *Experimental Principles and Methods below 1 K*, (Academic Press, New York, 1974).
- [22] F. Pobell, *Matter and Methods at Low Temperatures*, (Springer-Verlag, Berlin Heidelberg, 1992).
- [23] G. J. Labbe, H. Royce, Y. Takano, and G. G. Ihas, in G. G. Ihas and Y. Takano, editors, *Quantum Fluids and Solids*, (AIP, New York, 1989) page 395.
- [24] J. Xu, O. Avenel, J. S. Xia, M-F. Xu, T. Lang, P. L. Moyland, W. Ni, E. D. Adams, G. G. Ihas, M. W. Meisel, N. S. Sullivan, and Y. Takano. *J. Low Temp. Phys.* **89**, 719 (1992).
- [25] T. Lang Ph.D. Thesis, 1996, University of Florida (unpublished).
- [26] Y. Takano, *Rev. Sci. Instrum.* **65**, 1667 (1994).
- [27] R. M. Mueller, C. Buchal, T. Oversluizen, and F. Pobell. *J. Low Temp. Phys.* **49**, 515 (1978).
- [28] G. S. Straty and E. D. Adams, *Rev. Sci. Instrum.* **40**, 1393 (1969).
- [29] W. Ni, J. S. Xia, E. D. Adams, P. S. Haskins, and J. E. McKisson, *J. Low Temp. Phys.* **99**, 167 (1995).
- [30] E. D. Adams, *Rev. Sci. Instrum.* **64**, 601 (1993).
- [31] Th. Wagner, S. Gotz, and G. Eska, *Cryogenics* **34**, 655 (1994).
- [32] D. Hechtfisher, *Rev. Sci. Instrum.* **52**, 237 (1987).
- [33] Y. Takano, unpublished report.
- [34] J. Korringa, *Physica* **16**, 601 (1950).
- [35] P. Jauho and P. V. Pirila, *Phys. Rev B* **1**, 21 (1970).
- [36] F. Bacon, J. A. Barclay, W. D. Brewer, D. A. Shirley, and J. E. Templeton, *Phys. Rev. B* **5**, 2397 (1972).
- [37] F. Bloch, W. W. Hansen, and M. Packard, *Phys. Rev.*, **69**, 127 (1946).

- [38] D. E. MacLaughlin, *Rev. Sci. Instrum.* **41**, 1202 (1970).
- [39] J. A. Nelder and R. Mead, *Computer Journal* **7**, 308 (1986).
- [40] A. Narath, A. T. Fromhold, Jr., and E. D. Jones, *Phys. Rev.* **144**, 428 (1966).
- [41] Philip R. Bevington and D. Keith Robinson, *Data Reduction and Error Analysis for the Physical Sciences*, (McGraw-Hill, NY, 1992).
- [42] K. Andres, G. Eska, and S. Darack, *J. Phys. (Paris)* **39**, C6-1157 (1978).
- [43] K. Andres and O. V. Lounasmaa, in D. F. Brewer, editor, *Progress in Low Temperature Physics*, **8**, (North-Holland, Amsterdam 1982) page 221.
- [44] E. Bucher, J. P. Maita, G. W. Hull, R. C. Fulton, and A. S. Cooper, *Phys. Rev. B* **11**, 440 (1975).
- [45] M. J. Besnus, J. P. Kappler, B. Lemius, M. Benakki, and A. Meyer, *J. Appl. Phys.* **53**, 2158 (1982).
- [46] J. M. Bloch, D. Davidov, I. Felner, and D. Shaltiel, *J. Phys. F* **6**, 1979 (1976).
- [47] A. Hiess, M. Bonnet, P. Burlet, E. Ressouche, J. P. Sanchez, J. C. Waerenborgh, S. Zwirner, F. Wastin, J. Rebizant, G.H. Lander, and J. L. Smith, *Phys. Rev. Lett.* **77**, 3917 (1996).
- [48] R. H. Heffner *Phys. Rev. Lett.* **65**, 2816 (1990).
- [49] G. H. Lander, *Phys. Rev. B* **32**, 5387 (1992).
- [50] J. Xu, O. Avenel, J. S. Xia, M-F. Xu, T. Lang, P. L. Moyland, W. Ni, E. D. Adams, G. G. Ihas, M. W. Meisel, N. S. Sullivan, and Y. Takano, *J. Low Temp. Phys.* **49**, 719 (1992).
- [51] J. S. Smart, *Phys. Rev.* **86**, 968 (1952).
- [52] D. ter Haar and M. E. Lines, *Phil. Trans. Roy. Soc. London* **A245**, 1046 (1962).


BIOGRAPHICAL SKETCH

Paul Lee Moyland was born on March 27, 1966 in Columbus, Georgia. In 1984, he graduated from high school, and attended the University of California at Berkeley. Upon graduating from there in 1989 with degrees in physics and applied mathematics, he enrolled in the graduate program in physics at the University of Florida. He plans to graduate in May of 1997.

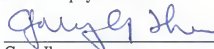
I certify that I have read this study and that in my opinion it conforms to acceptable standards of scholarly presentation and is fully adequate, in scope and quality, as a dissertation for the degree of Doctor of Philosophy.


Yasumasa Takano, Chairman
Professor of Physics


I certify that I have read this study and that in my opinion it conforms to acceptable standards of scholarly presentation and is fully adequate, in scope and quality, as a dissertation for the degree of Doctor of Philosophy.


Neil S. Sullivan
Professor of Physics


I certify that I have read this study and that in my opinion it conforms to acceptable standards of scholarly presentation and is fully adequate, in scope and quality, as a dissertation for the degree of Doctor of Philosophy.


Gary Ihas
Professor of Physics

I certify that I have read this study and that in my opinion it conforms to acceptable standards of scholarly presentation and is fully adequate, in scope and quality, as a dissertation for the degree of Doctor of Philosophy.


Pradeep Kumar
Professor of Physics

I certify that I have read this study and that in my opinion it conforms to acceptable standards of scholarly presentation and is fully adequate, in scope and quality, as a dissertation for the degree of Doctor of Philosophy.


William Weltner
Professor of Chemistry

This dissertation was submitted to the Graduate Faculty of the Department of Physics in the College of Liberal Arts and Sciences and to the Graduate School and was accepted as partial fulfillment of the requirements for the degree of Doctor of Philosophy.

May 1997

Dean, Graduate School